OCS Study MMS 2001-069

Numerical Simulation of Atmosphere/Ocean/Sea Ice Interaction in the Arctic Ocean: 1982–1996

Dale B. Haidvogel
Institute of Marine and Coastal Sciences
Rutgers University

Katherine S. Hedström
Institute of Marine and Coastal Sciences
Rutgers University

Jennifer Francis
Institute of Marine and Coastal Sciences
Rutgers University

October 2001

This study was funded by the Alaska Outer Continental Shelf Region of the Minerals Management Service, U.S. Department of the Interior, Anchorage, Alaska, through Contract **14-35-01-96-CT-30818** with Rutgers University, Institute of Marine and Coastal Sciences.

This document was prepared with LaTeX and **xfig**.

Acknowledgments

Development and testing of the SCRUM model has been funded by the Minerals Management Service (14-35-01-96-CT-30818) and the Office of Naval Research (N00014-93-1-0758, N00014-95-1-0457, and N00014-93-1-0197). Computational resources for the simulations described here were provided by the Naval Research Laboratory (NRL) in Washington, DC. The authors thank the NRL and its staff for their support.

Joseph Cermak assisted in obtaining access to the large amount of TOVS PathP data and in making sure we got the winds going in the right direction. The comparison files from buoys were obtained from the Applied Physical Laboratory in Seattle. Ignatius Rigor was very helpful and prompt in making these file available via the WWW. The ice model used is a combination of the ice dynamics model from Paul Budgell and the ice thermodynamics from Sirpa Häkkinen. Paul was kind enough to allow us to be one of the very early users of his model. We obtained Sirpa's model via Paul and his Norwegian colleagues, who call it "hakkis".

This is Contribution #2000-07 of the Institute of Marine and Coastal Sciences, Rutgers University.

Abstract

We describe a multi-year hindcast of coupled circulation/sea ice evolution in the Arctic Ocean. This study extends that described in Hedström *et al.* [26]. Its technical goals include: 1) the implementation of several important improvements in the coupled circulation/sea ice model; 2) the expansion of the model geometry to include both the entire Arctic Ocean, and the entire water column depth; 3) the development and utilization of enhanced spatial resolution and higher quality atmospheric forcing products; 4) the improvement of the parameterization used for ocean surface layer mixing; and finally, 5) the extension of the model simulation to encompass the entire 15-year hindcast period from 1982 through 1996. These goals – which substantially improve the sophistication and realism of the model hindcasts – have been met.

A principal scientific goal has been the retrospective simulation of surface circulation and sea ice fields, with particular interest in the patterns of interannual and (potentially) systematic variability, and the comparison of these hindcast fields with available datasets and previous model results. In particular, our 15-year coupled model hindcasts are consistent with the large-scale circulation features and sea ice distributions within the Arctic Ocean, to the extent that quantitative datasets exist for validation. Importantly, the bulk properties of the sea ice distribution observed during 1982-1996 – including ice concentration, thickness and motion, and their interannual variations – are reproduced well by the coupled model. In addition to prominent year-to-year variations in (*e.g.*) the strength of the Beaufort Gyre and the associated sea ice motion, there are also strong progressive changes in sea ice properties, as has been noted in other recent studies.

Contents

List of Figures

List of Tables

1 Introduction

1.1 Oceanographic setting

The Arctic Ocean extends over an area of approximately 9×10^6 km^2 and consists of two major deep (≥ 3000 m) basins, the Canadian and the Eurasian, which are fringed by shallow shelf areas. The basins are separated by the Lomonosov ridge over which the depth is roughly 1000 m. The continental shelves occupy nearly one third of the total Arctic Ocean area and vary in width from approximately 40 km at the Alaskan coast (Beaufort Sea), to about 800 km at the Siberian coast. The Arctic Ocean is connected to adjacent seas by the Bering Strait, an open border in the Barents Sea, the Fram Strait, and a number of narrow passages in the Canadian Archipelago.

The circulation in the Arctic Ocean is primarily driven by strong atmospheric forcing, the large amount of fresh water runoff, and property exchanges with the North Pacific and North Atlantic Oceans. In addition, the Arctic circulation is influenced by its complex bathymetry, and the effects of perennial and seasonal ice cover. The effects of sea ice on the circulation are primarily related to the role played by the ice in the transfer of momentum from the atmosphere to the ocean, and to the thermohaline effects associated with brine rejection during freezing.

Figure 1 (AMAP [6]) depicts the geometry and subsurface circulation of the Arctic Ocean. This figure shows areas of strong boundary currents, the shallow exchanges with the North Atlantic and North Pacific oceans, potential saline source areas, and areas likely to have long-lived baroclinic eddies. A distinctive feature of the western Arctic circulation is the Beaufort Gyre, which is a large-scale anticyclone. The Beaufort Sea contains the westward branch of the gyre.

At least below the upper $40 - 50$ m, the principal kinematic feature over the outer shelf and slope of the Beaufort Sea is the Beaufort Undercurrent, a strong flow which in the mean is directed eastward, but which is subject to frequent (three to ten day) reversals toward the west. The reversals are normally associated with upwelling onto the outer shelf. The undercurrent is very likely part of a basin-scale circulation within the Arctic Ocean. Despite the seasonally varying wind field, as well as the large seasonal differences in the upper-ocean temperature and salinity fields, there is no evidence for a significant seasonal variability in the subsurface circulation in the Beaufort Sea (Aagaard [4]). However, the wind forcing influence, and therefore the seasonal variability, is much stronger near the surface where as much as 50% of the flow variability is wind related.

Björk [7] provides a concise review of the vertical structure in the Arctic Ocean compiled from Threshnikov and Baranov [53]. The upper layer of the Arctic Ocean is characterized by a mixed layer of thickness between 25 and 50 m and temperature near the freezing point. The salinity increases horizontally from about 30 PSU in the Beaufort Sea, to about 32 PSU near the Fram Strait. Below the mixed layer is a halocline where the salinity increases to about 34 PSU at 100 m depth, while the temperature is still near the freezing point. Below the halocline the temperature increases and attains a maximum with temperatures above 0 C. The corresponding layer is called the Atlantic layer, and has a salinity of about 34.8 PSU. The upper boundary of the Atlantic Layer is situated approximately at 300 m in the Beaufort Sea and rises to near 200 m near Greenland. The maximum temperature is between 0.4 and 1 C over most parts of the basin with the warmest water near the Fram Strait. The thickness of the Atlantic layer ranges between 500 and 800 m. Below the Atlantic layer the water is relatively homogeneous with temperature between 0 and -0.9 C, and salinity in the range of 34.90 and 34.95 PSU.

1.2 Sea ice

The study of the seasonal and interannual variability of sea ice in the Arctic Ocean and adjacent seas began in the early 1970's when hemispheric-scale observations of sea ice cover became possible. All records prior to that time are spatially very incomplete. Parkinson [40], using passive microwave

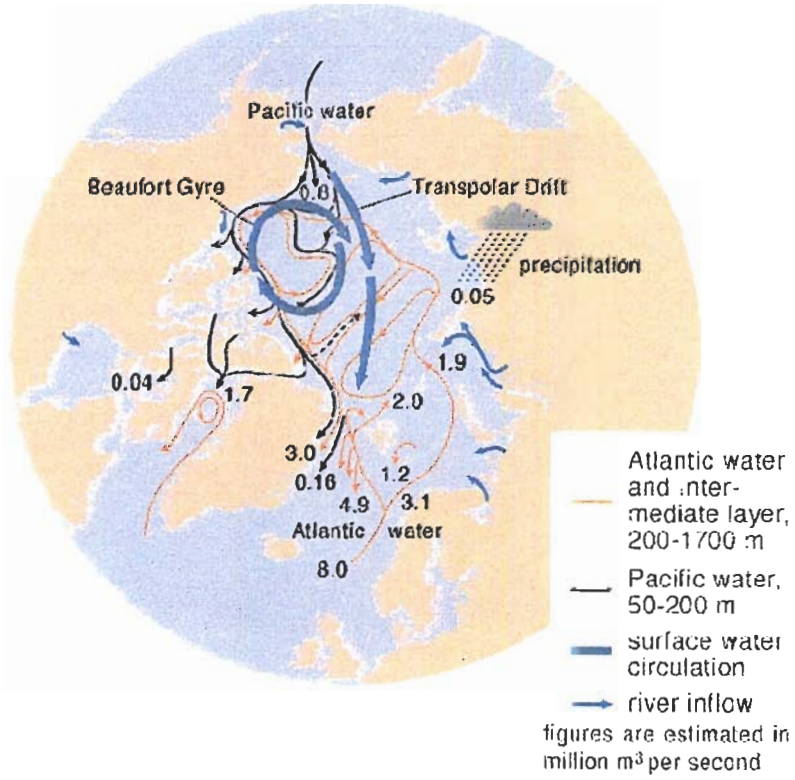

Figure 1: Overview of the Arctic circulation.

data from the Nimbus 5 and Nimbus 7 satellites, determined baseline information on the interannual variability in monthly averaged sea ice distributions in the north polar region over the period 1973-1987, as summarized below. Additional literature on the variability and distribution of ice in the Arctic for this period is also available in Walsh and Johnson [57], Walsh *et al.* [56], Bourke and Garrett [9], Campbell *et al.* [10], Hibler [27], Semtner [3].

The spatial distributions of the ice in the Arctic Ocean and Canadian Archipelago have their lowest variability in winter and highest variability in summer. Both regions are fully ice covered in the central winter months to at least 30% ice concentration in each of the 15 years analyzed. Although both regions retain considerable ice coverage throughout the year, the spatial distributions of the summertime coverage can vary substantially from year to year. In both regions the highest interannual variability is in September, and the second highest in August. There is a sharp drop in variability from September to October, reflecting the consistency with which winter-like conditions have set in by the end of October.

Much of the summer-time variability in the Arctic Ocean results from different patterns of ice distribution rather than from changes in areal ice extent. This is substantiated by a census of summer-time ice coverage from year-to-year, which indicates that the total areal coverage of ice in different summers is sometimes very close even though the distributions of the ice vary considerably. For example, the Arctic Ocean ice extents in September 1973 and September 1974 differed by only 2%, although in 1973 there was a wide strip of open water north of Alaska and Canada eastward to $125^{o}W$ which did not exist in 1974. In contrast, there was much more open water north of Svalbard and north of eastern Siberia in 1974 than in 1973. These September 1973-1974 contrasts can be explained on the basis of ice responses to the different atmospheric forcings in the 2 years.

A more recent comparison of submarine-observed Arctic sea ice draft from the 1960s with data from the 1990s (Rothrock *et al.* [45]) reveals a cohesive picture of ice thinning across the Arctic Basin – approximately 40% on average. In addition, during the past few decades, the areal extent of Arctic sea-ice cover has decreased (Cavalieri *et al.* [11]), and ice fluxes and flow patterns have changed (Kwok [31]), Kwok and Rothrock [32]). Smith ([49]) finds that the Arctic melt season has lengthened since 1979, perhaps owing to an increase in net surface radiation. At present the cause of these apparent trends is unknown, but a change in the advected heat into the Arctic is a likely candidate.

1.3 The role of the Arctic atmosphere

The Arctic Oscillation (AO) has recently been identified as a fundamental mode of variability of the Arctic atmosphere (Thompson and Wallace [51]). However, it is unclear how variations in the AO affect regional conditions in the Arctic. Poleward transport of heat and moisture constitutes the primary link between the Arctic and the global circulation system (*e.g.*, Nakamura and Oort [38]), thus we would expect to find strong linkages between the AO and patterns of advection into and within the Arctic, as well as consequent interactions with cloud and surface properties (*e.g.*, sea ice). While global circulation models agree that variability is enhanced in the polar regions, their ability to replicate present climate patterns varies widely, particularly at high latitudes. One of the primary causes of these differences is believed to be unrealistic representations of energy exchange processes between the atmosphere and sea ice.

Dramatic changes in a wide variety of atmospheric, cryospheric, oceanic, and biological variables have been observed during this period by numerous investigators (*e.g.*, Dickson [15]; Serreze *et al.* [48]). For example, the AO exhibits a significant jump from a negative to a positive regime near 1989 (Overland *et al.* [39]). An accompanying change in the low-level flow field is reported by Walsh *et al.* ([55]), which is believed to be related to observed changes in sea ice extent (Cavalieri *et al.* [11], Wang and Ikeda [58]) and sea ice motion fields (Kwok [31]). In the past

decade, extreme and unprecedented (in the available data record) minima in ice extent have been observed in certain regions of the Arctic Ocean during 1990, 1993, 1995, and 1998 (Maslanik *et al.* [35], Maslanik *et al.* [34]). In all four of these years with unusually low ice extent, the causes are presumed to be some combination of anomalies in offshore wind stress and atmospheric advection of warm air. Our preliminary calculations indicate that significant, cohesive changes have indeed occurred in advection patterns during recent decades, including significant differences in the poleward component of advective heating in the upper troposphere between the 1990s and 1980s.

The importance of lateral energy advection to the evolution of sea ice is illustrated in a simple coupled ice/atmosphere model by Thorndike [52]. Based on his model behavior, Thorndike speculates that relatively small changes in advection can cause large differences in the mean sea-ice thickness; only a few tens of watts per square meter can transform the modeled Arctic from present-day conditions to an ice-free ocean. While he stresses that these values may be incorrect in absolute terms owing to the simplicity of his model, the results do suggest that the Arctic climate is extremely sensitive to changes in its primary energy conduit. Unfortunately, the energy budget in high latitudes is particularly challenging to observe and model, as interannual variability is large, interactions are complex, and validation is difficult. Understanding these processes is essential for determining why the Arctic has recently changed so rapidly and for assessing how these patterns of change and related parameters may evolve.

1.4 Previous coupled simulations

A prognostic two-dimensional model was used by Kantha and Mellor [30] to study the evolution of the coupled ice-ocean behavior in the Bering Sea. They found that the density structure and the circulation beneath the ice, and the position of the ice edge, are quite sensitive to even small changes in the relevant parameters governing the dynamics and thermodynamics of the system. Several three-dimensional coupled ice-ocean models have been developed for the Arctic Ocean and adjacent seas. Some relevant examples are the Semtner [3] model, which treats both the ice and ocean prognostically, and the Hibler and Bryan [29] study, where the ocean is treated diagnostically.

Fleming and Semtner [18] conducted a fully prognostic study of the Arctic ice cover using a coupled ice-ocean model (horizontal resolution of 100 km) described by Fleming [17]. The coupled model system consists of the Semtner [2] ocean model combined with the three-layer thermodynamic ice model (Semtner [1]) and a modified Hibler [27] dynamic ice model. The study shows that the vertical ocean heat flux appears to be the dominant mechanism controlling localized ice area anomalies and the overall ice concentration. The model produces very reasonable simulations of the ice edge position, particularly in the Barents and Greenland seas. However, consistent errors in simulated ice concentration are identified in the numerical study, including an exaggerated melt-freeze cycle and insufficient ice thickness. The authors point out that the lack of a mixed layer formulation in the model dynamics, and the coarse vertical resolution (20 to 30 m in the upper layers for these experiments), are inadequate to properly represent the processes related to the ocean's heat flux (*e.g.*, vertical mixing, stratification and diffusion).

Piacsek *et al.* [42] studied the Arctic ice cover and upper ocean with a coupled ice-ocean model. The model uses the Hibler ice model coupled to a three-dimensional ocean model that consists of a turbulent mixed layer (Mellor and Yamada [37]) and an inverse geostrophic model. The horizontal grid resolution adopted is approximately 127 km, and the vertical grid resolution ranges from 2.5 m near the surface to 1700 m near the bottom. The model is forced with 12-hourly GCM-derived (Naval Polar Oceanography Center) atmospheric fluxes for the year 1986, for which good quality ice edge analyses and observed Arctic buoy tracks (Colony and Rigor [14]) were available for comparisons. In general, the computed ice edge positions from the model have comparable accuracy to previous three-dimensional coupled ice-ocean studies, with too much ice growth during

the winter in the Barents Sea and too little ice east of Greenland. However, some improvements in the ice thickness distributions were achieved, with a monotonic increase of the ice thickness from the Siberian coast east toward the Canadian archipelago with a maximum winter values of 5–6 m. There is generally close agreement between the model and observed buoy positions, but the model tracks exhibit some loops which are missing in the observed track. The authors suggest that further improvements in the modeled buoy tracks can be achieved by an increase in the horizontal model resolution, an improvement of the atmospheric forcing (higher resolution winds), and the use of a fully prognostic (ageostrophic) momentum cycle.

Häkkinen [24] simulated the Arctic ice-ocean system by coupling the Semtner [1] ice model to the sigma coordinate ocean model described by Blumberg and Mellor [8]. The horizontal resolution for the adopted orthogonal grid ranges from 28 to 150 km; there are 18 sigma levels in the vertical grid. The model focuses on the interannual variability of the sea ice during the period 1955-1975. The main conclusion is that the model results show the origin of the Great Salinity Anomaly (GSA) to be in the Arctic, as suggested by Aagaard and Carmack [5] and support the view that the Arctic may play an active role in climate change. The extensive ice cover of 1968 has been widely speculated as the source of the GSA, a high-latitude freshwater event which circulated during the 1970's around the subpolar gyre and returned to the Greenland Sea in the early 1980's (Dickson *et al.* [16]).

In an earlier version of the present study (Hedström *et al.* [26]), a coupled ocean circulation / sea ice model was used to simulate flow properties and sea ice evolution in the Western Arctic during the year 1983. The coupled model – based upon the semi-spectral primitive equation model of Haidvogel *et al.* [23] and the Hibler [27] sea ice model – was implemented on a uniform 20 km grid over the Western Arctic, and utilized forcing by daily surface geostrophic winds and monthly averaged thermodynamic fluxes. The results of the model simulation were shown to be consistent with the large-scale circulation features of the Western Arctic. In particular, the Beaufort Gyre and its seasonal variability in the sense and amplitude of its circulation were reproduced to the extent of our ability to quantify them in the target year of 1983. The bulk properties of the ice distribution observed during 1983 – including ice concentration and thickness and its seasonal growth and retreat – were also reproduced well by the coupled model to the degree that available observations allowed model evaluation. Some systematic tendency for faster-than-observed melting in the spring and summer months was seen in the model along the Siberian continental shelf. The poorest model performance was obtained in the comparison between the model-inferred ice floe ("float") trajectories and the observed trajectories of surface floats released in the Arctic in 1983. Mean motion of the simulated drifters was found to be comparable to those observed; however, little agreement between individual sets of trajectories was obtained.

1.5 Organization of this report

The remainder of this report is organized as follows. Section 2 provides a brief overview of the formulation of the coupled circulation / sea ice model. (The reader is referred to the accompanying technical manual – Hedström [25] – for a complete description of the coupled system.) Section 3 discusses the properties of the new atmospheric forcing dataset being used for the first time in this study. The configuration and parametric features of the 15-year retrospective simulation are described in Section 4. Results of the simulation are discussed and compared with available contemporaneous observations in Section 5. Finally, a concluding Section summarizes model performance and offers some suggestions on where to look for further improvements in the future.

2 Formulation of the coupled model

Many improvements to the versatility and realism of the coupled model have been implemented in version 2. These include, but are not limited to, the following: the addition to the circulation model of an active sea surface and a state-of-the-art surface mixing parameterization (Large *et al.* [33]), and the incorporation within the sea ice model of improved thermodynamics and a more robust elliptic solver for the ice mechanics. The latter also allows utilization of the coupled model on curvilinear grids, as discussed further below.

2.1 Equations of oceanic motion

The primitive equations in Cartesian coordinates can be written:

$$\frac{\partial u}{\partial t} + \vec{v} \cdot \nabla u - fv = -\frac{\partial \phi}{\partial x} + \mathcal{F}_u + \mathcal{D}_u \tag{1}$$

$$\frac{\partial v}{\partial t} + \vec{v} \cdot \nabla v + fu = -\frac{\partial \phi}{\partial y} + \mathcal{F}_v + \mathcal{D}_v \tag{2}$$

$$\frac{\partial T}{\partial t} + \vec{v} \cdot \nabla T = \mathcal{F}_T + \mathcal{D}_T \tag{3}$$

$$\frac{\partial S}{\partial t} + \vec{v} \cdot \nabla S = \mathcal{F}_S + \mathcal{D}_S \tag{4}$$

$$\rho = \rho(T, S, P) \tag{5}$$

$$\frac{\partial \phi}{\partial z} = \frac{-\rho g}{\rho_o} \tag{6}$$

$$\frac{\partial u}{\partial x} + \frac{\partial v}{\partial y} + \frac{\partial w}{\partial z} = 0. \tag{7}$$

The variables are shown in Table 1.

Variable	Value (if constant)	Description
g	$9.81\, m\, s^{-2}$	acceleration of gravity
$\mathcal{D}_u, \mathcal{D}_v, \mathcal{D}_T, \mathcal{D}_S$		diffusive terms
$\mathcal{F}_u, \mathcal{F}_v, \mathcal{F}_T, \mathcal{F}_S$		forcing terms
$f(x,y)$		Coriolis parameter
$h(x,y)$		bottom depth
ν, κ		horizontal viscosity and diffusivity
K_m, K_T, K_S		vertical viscosity and diffusivity
P		total pressure $P \approx -\rho_o g z$
$\phi(x,y,z,t)$		dynamic pressure $\phi = (P/\rho_o)$
$\rho_o + \rho(x,y,z,t)$		total *in situ* density
$S(x,y,z,t)$		salinity
t		time
$T(x,y,z,t)$		potential temperature
u, v, w		the (x,y,z) components of vector velocity $\vec{v}$
x, y		horizontal coordinates
z		vertical coordinate
$\zeta(x,y,t)$		the surface elevation

Table 1: The variables used in the description of the ocean model

Equations (1) and (2) express the momentum balance in the x- and y-directions, respectively. The time evolution of the potential temperature and salinity fields, $T(x,y,z,t)$ and $S(x,y,z,t)$, are governed by the advective-diffusive equations (3) and (4). The equation of state is given by equation (5). In the Boussinesq approximation, density variations are neglected in the momentum equations except in their contribution to the buoyancy force in the vertical momentum equation (6). Under the hydrostatic approximation, it is further assumed that the vertical pressure gradient balances the buoyancy force. Lastly, equation (7) expresses the continuity equation for an incompressible fluid. For the moment, the effects of forcing and dissipation will be represented by the schematic terms $\mathcal{F}$ and $\mathcal{D}$, respectively.

In the absence of sea ice, the vertical boundary conditions at the (moving) surface and at the bottom are prescribed as follows:

$$
\begin{aligned}
\text{top } (z = \zeta(x,y,t)) \qquad & K_m \tfrac{\partial u}{\partial z} = \tau_s^x(x,y,t) \\
& K_m \tfrac{\partial v}{\partial z} = \tau_s^y(x,y,t) \\
& K_T \tfrac{\partial T}{\partial z} = \tfrac{Q_T}{\rho_o c_P} \\
& K_S \tfrac{\partial S}{\partial z} = \tfrac{(E-P)S}{\rho_o} \\
& w = \tfrac{\partial \zeta}{\partial t} \\
\text{and bottom } (z = -h(x,y)) \qquad & K_m \tfrac{\partial u}{\partial z} = \tau_b^x(x,y,t) \\
& K_m \tfrac{\partial v}{\partial z} = \tau_b^y(x,y,t) \\
& K_T \tfrac{\partial T}{\partial z} = 0 \\
& K_S \tfrac{\partial S}{\partial z} = 0 \\
& -w + \vec{v} \cdot \nabla h = 0 \ .
\end{aligned}
$$

Variable	Value (if constant)	Description
γ_1, γ_2	$4.5 \times 10^{-4}\ m\,s^{-1}$, 3×10^{-3}	linear and quadratic bottom stress coefficients
$E - P$		evaporation minus precipitation
Q_T		surface heat flux
τ_s^x, τ_s^y		surface wind stress
τ_b^x, τ_b^y		bottom stress

Table 2: The variables used in the vertical boundary conditions for the ocean model

The surface boundary condition variables are defined in Table 2. On the variable bottom, $z = -h(x,y)$, the horizontal velocity components are constrained to accommodate a prescribed bottom stress which is a sum of linear and quadratic terms:

$$
\begin{aligned}
\tau_b^x &= (\gamma_1 + \gamma_2 \sqrt{u^2 + v^2})u \\
\tau_b^y &= (\gamma_1 + \gamma_2 \sqrt{u^2 + v^2})v \ .
\end{aligned}
$$

The vertical heat and salt flux may also be prescribed at the bottom, although here they are set to zero.

2.2 Ice Model Formulation

Hibler [27] has described a model for the simulation of sea ice circulation and thickness. Although no longer the only sea ice model in existence, it is nonetheless still the standard approach used for coupled simulations on the scales addressed here. Our version of the Hibler model has been rewritten

by Paul Budgell and is now implemented on an orthogonal, curvilinear Arakawa C-grid, has a new elliptic solver, and the nonlinear advection of momentum has been omitted. The thermodynamics are derived from Mellor and Kantha [36] (MK89 below). Sirpa Häkkinen allowed us to use her implementation of MK89; we obtained it from the Norwegians, who call it "hakkis".

2.2.1 Momentum balance

The overall structure consists of two principal components—the momentum equations and the ice continuity equations. The momentum balance includes air and water stress, Coriolis force, internal ice stress, inertial forces and ocean tilt as shown in equations (8) and (9):

$$M\frac{\partial u}{\partial t} = Mfv - Mg\frac{\partial \zeta_w}{\partial x} + \tau_a^x + \tau_w^x + \mathcal{F}_x \tag{8}$$

$$M\frac{\partial v}{\partial t} = -Mfu - Mg\frac{\partial \zeta_w}{\partial y} + \tau_a^y + \tau_w^y + \mathcal{F}_y. \tag{9}$$

The nonlinear advection terms have been omitted, since they are usually much smaller than the others. Nonlinear formulas are used for both the ocean-ice and air-ice surface stress:

$$\vec{\tau}_a = \rho_a C_a |\vec{V}_{10}|\vec{V}_{10} \tag{10}$$

$$C_a = \frac{1}{2}C_d[1 - \cos(2\pi \min(h_i + .1, .5))] \tag{11}$$

$$\vec{\tau}_w = \rho_w C_w |\vec{v}_w - \vec{v}|(\vec{v}_w - \vec{v}). \tag{12}$$

The symbols used in these equations along with the values for the constants are listed in Table 3.

A key component of the momentum balance is the force due to the internal ice stress ($\mathcal{F}_x$ and $\mathcal{F}_y$). This force is based on a constitutive law which relates the ice stress to the strain rate and ice strength (equation (13)). For this model, a viscous-plastic behavior is used. Rigid plastic behavior is approximated in this law by allowing the ice to flow in a plastic manner for normal strain rates and to creep in a linear viscous manner for small strain rates. The treatment of ice as a viscous-plastic fluid was largely motivated by the desire to avoid the complexities associated with elastic-plastic behavior under flow. The stress-strain relationship is given by

$$\sigma_{ij} = 2\eta\epsilon_{ij} + (\zeta - \eta)\epsilon_{kk}\delta_{ij} - \frac{P}{2}\delta_{ij}. \tag{13}$$

The viscous-plastic terms (15) and (16) are found by taking the divergence of the stress tensor:

$$(\mathcal{F}_x, \mathcal{F}_y) = \nabla \cdot \boldsymbol{\sigma} \tag{14}$$

with the result that

$$\mathcal{F}_x = \frac{\partial}{\partial x}\left[(\eta + \zeta)\frac{\partial u}{\partial x} + (\zeta - \eta)\frac{\partial v}{\partial y} - P/2\right] + \frac{\partial}{\partial y}\left[\eta\left(\frac{\partial u}{\partial y} + \frac{\partial v}{\partial x}\right)\right] \tag{15}$$

$$\mathcal{F}_y = \frac{\partial}{\partial y}\left[(\eta + \zeta)\frac{\partial v}{\partial y} + (\zeta - \eta)\frac{\partial u}{\partial x} - P/2\right] + \frac{\partial}{\partial x}\left[\eta\left(\frac{\partial u}{\partial y} + \frac{\partial v}{\partial x}\right)\right] \tag{16}$$

where the nonlinear viscosities are given by

$$\zeta = \frac{P}{2\left[(\epsilon_{11}^2 + \epsilon_{22}^2)(1 + 1/e^2) + 4e^{-2}\epsilon_{12}^2 + 2\epsilon_{11}\epsilon_{22}(1 - 1/e^2)\right]^{1/2}} \tag{17}$$

and

$$\eta = \frac{\zeta}{e^2}. \tag{18}$$

Variable	Value (if constant)	Description
C_d	2.2×10^{-3}	air drag coefficient
C_w	10×10^{-3}	water drag coefficient
e	2	eccentricity of the elliptical yield curve
g	$9.81\, m\, s^{-2}$	acceleration of gravity
(P^*, C)	$(2.75 \times 10^4, 20)$	ice strength parameters
(ρ_a, ρ_w)	$(1.3\, kg\, m^{-3}, 1025\, kg\, m^{-3})$	air and water densities
$A(x,y,t)$		ice concentration
$\alpha(A)$		ridging function
C_a		nonlinear air drag coefficient
$(\mathcal{D}_h, \mathcal{D}_s, \mathcal{D}_A)$		diffusion terms
$\epsilon_{ij}(x,y,t)$		strain rate tensor
$\eta(x,y,t)$		nonlinear shear viscosity
$(\mathcal{F}_x, \mathcal{F}_y)$		internal ice stress
$f(x,y)$		Coriolis parameter
H		Heaviside function
$h_i(x,y,t)$		ice thickness of ice-covered fraction
$h_s(x,y,t)$		snow thickness on ice-covered fraction
$M(x,y,t)$		ice mass (density times thickness)
$P(x,y,t)$		ice pressure or strength
(S_h, S_s, S_A)		thermodynamic terms
$\sigma_{ij}(x,y,t)$		stress tensor
$\vec{\tau}_a$		air stress
$\vec{\tau}_w$		water stress
(u,v)		the (x,y) components of ice velocity $\vec{v}$
$(\vec{V}_{10}, \vec{v}_w)$		10 meter air and surface water velocities
$\zeta(x,y,t)$		nonlinear bulk viscosity
$\zeta_w(x,y,t)$		height of the ocean surface

Table 3: Variables used in the ice momentum equations

The "pressure gradient" term is also modeled as a term in the internal ice stress. This term represents the resistance which ice has to being compressed (ice strength) and is a function of ice thickness and concentration:

$$P = P^* A h_i \exp[-C(1-A)] H(-\nabla \cdot \vec{v}) \; . \tag{19}$$

The Heaviside function guarantees that the ice has no strength when the flow is divergent (Gray and Killworth [21]).

The second major component of the model consists of continuity equations describing the evolution of the ice thickness characteristics. Three parameters are calculated: the ice thickness h_i, the snow thickness h_s, and the compactness, A, which is defined as the fraction of area covered by thick ice. The continuity equations describing the evolution of these parameters (equations (20)–(22)) also include thermodynamic terms (S_h, S_s and S_A), which will be described in §2.2.2:

$$\frac{\partial A h_i}{\partial t} = -\frac{\partial (u A h_i)}{\partial x} - \frac{\partial (v A h_i)}{\partial y} + S_h + \mathcal{D}_h \tag{20}$$

$$\frac{\partial A h_s}{\partial t} = -\frac{\partial (u A h_s)}{\partial x} - \frac{\partial (v A h_s)}{\partial y} + S_s + \mathcal{D}_s \tag{21}$$

$$\frac{\partial A}{\partial t} = -\frac{\partial (u A)}{\partial x} - \frac{\partial (v A)}{\partial y} + S_A + \mathcal{D}_A \qquad 0 \le A \le 1. \tag{22}$$

The first two equations represent the conservation of ice and snow. Equation 22 is discussed in some detail in MK89, but represents the advection of ice blocks in which no ridging occurs as long as there is any open water. An optional ridging term can be added (Gray and Killworth [22]):

$$\frac{\partial A}{\partial t} = -\frac{\partial (u A)}{\partial x} - \frac{\partial (v A)}{\partial y} - A\alpha(A) \nabla \cdot \vec{v} H(-\nabla \cdot \vec{v}) + S_A + \mathcal{D}_A \qquad 0 \le A \le 1. \tag{23}$$

where $\alpha(A)$ is an arbitrary function such that $\alpha(0) = 0$, $\alpha(1) = 1$, and $0 \le \alpha(A) \le 1$. The ridging term leads to an increase in h_i under convergent flow as would be produced by ridging. The function $\alpha(A)$ should be chosen so that it is near zero until the ice concentration is large enough that ridging is expected to occur, then should increase smoothly to one.

2.2.2 Thermodynamics

The thermodynamics used is based on the algorithm described in Mellor and Kantha [36], who have a useful description of the various melting and freezing processes, plus the coupling to a full three-dimensional ocean. Their form of equations (20) and (22) is:

$$\frac{\partial A h_i}{\partial t} + \frac{\partial (u A h_i)}{\partial x} + \frac{\partial (v A h_i)}{\partial y} = \frac{\rho_o}{\rho_i} [A(W_{io} - W_{ai}) + (1-A) W_{ao} + W_{fr}] \tag{24}$$

$$\frac{\partial A}{\partial t} + \frac{\partial (u A)}{\partial x} + \frac{\partial (v A)}{\partial y} = \frac{\rho_o A}{\rho_i h_i} [\Phi(1-A) W_{ao} + (1-A) W_{fr}] \qquad 0 \le A \le 1. \tag{25}$$

Here, the W variables are the freeze or melt rates as shown in Fig. 2 and Table 4. The frazil ice growth W_{fr} will be discussed further in §2.4—note that it contributes to changes in A as well as to changes in h_i. The other term that contributes to A is W_{ao}. This term includes a factor Φ which Mellor and Kantha set to different values depending on whether ice is melting or freezing:

$$\Phi = 4.0 \qquad W_{ao} \ge 0 \tag{26}$$

$$\Phi = 0.5 \qquad W_{ao} < 0 \tag{27}$$

Variable	Value (if constant)	Description
α_w	0.10	shortwave albedo of water
α_i	0.50	shortwave albedo of ice
α_s	0.75	shortwave albedo of snow
C_{pi}	2093 J kg^{-1} K^{-1}	specific heat of ice
C_{pw}	3987 J kg^{-1} K^{-1}	specific heat of water
ϵ_w	0.97	longwave emissivity of water
ϵ_i	0.97	longwave emissivity of ice
ϵ_s	0.99	longwave emissivity of snow
k_i	2.04 W m^{-1} K^{-1}	thermal conductivity of ice
k_s	0.31 W m^{-1} K^{-1}	thermal conductivity of snow
L_i	302 MJ m^{-3}	latent heat of fusion of ice
L_s	110 MJ m^{-3}	latent heat of fusion of snow
m	-0.054°C/PSU	coefficient in linear $T_f(S) = mS$ equation
ρ_i	910 m^3/kg	density of ice
S_i	5 PSU	salinity of the ice
σ	5.67×10^{-8} W m^{-2} K^{-4}	Stefan-Boltzmann constant
$T_{\text{melt\_s}}$	0° C	melting temperature of snow
C_k		snow correction factor
$E(T, r)$		enthalpy of the ice/brine system
$F_T\uparrow$		heat flux from the ocean into the ice
$H\downarrow$		sensible heat
i_w		fraction of the solar heating transmitted through a lead into the water below
$LE\downarrow$		latent heat
$LW\downarrow$		incoming longwave radiation
Φ		contribution to A equation from freezing water
Q_{ai}		heat flux out of the snow/ice surface
Q_{ao}		heat flux out of the ocean surface
Q_{i2}		heat flux up out of the ice
Q_{io}		heat flux up into the ice
Q_s		heat flux up through the snow
r		brine fraction in ice
$SW\downarrow$		incoming shortwave radiation
T_0		temperature of the bottom of the ice
T_1		temperature of the interior of the ice
T_2		temperature at the upper surface of the ice
T_3		temperature at the upper surface of the snow
T_f		freezing temperature
$T_{\text{melt\_i}}$	mS_i	melting temperature of ice
W_{ai}		melt rate on the upper ice/snow surface
W_{ao}		freeze rate at the air/water interface
W_{fr}		rate of frazil ice growth
W_{io}		freeze rate at the ice/water interface
W_{ro}	W_{ai}	rate of run-off of surface melt water

Table 4: Variables used in the ice thermodynamics

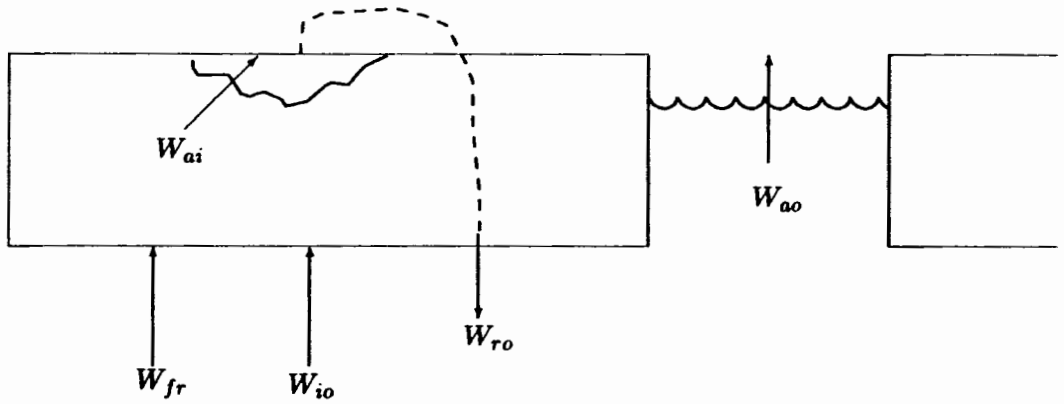

Figure 2: Diagram of the different locations where ice melting and freezing can occur.

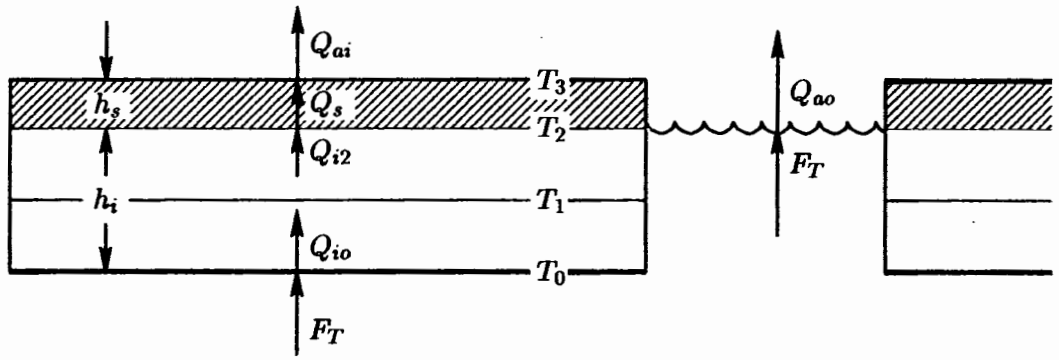

Figure 3: Diagram of internal ice temperatures and fluxes. The hashed layer is the snow.

Figure 3 shows the locations of the ice and snow temperatures and the heat fluxes. The temperature profile is assumed to be linear between adjacent temperature points. The interior of the ice contains "brine pockets", leading to a prognostic equation for the temperature T_1.

The surface flux to the air is:

$$Q_{ai} = -H\downarrow - LE\downarrow - \epsilon_s LW\downarrow - (1-\alpha_s)SW\downarrow + \epsilon_s \sigma (T_3 + 273)^4 \ . \tag{28}$$

The formulas for sensible heat, latent heat, and incoming longwave and shortwave radiation fluxes are the same as in Parkinson and Washington [41]. The sensible heat is a function of T_3, as is the heat flux through the snow Q_s. Setting $Q_{ai} = Q_s$, we can solve for T_3 by setting $T_3^{n+1} = T_3^n + \Delta T_3$ and linearizing in ΔT_3. The temperature T_3 is found by an iterative solution of the surface heat flux balance (using the previous value of T_1 in equation 36). As in Parkinson and Washington, if T_3 is found to be above the melting temperature, it is set to $T_{\rm melt}$ and the extra energy goes into melting the snow or ice:

$$W_{ai} = \frac{Q_{ai} - Q_{i2}}{\rho_o L_3} \tag{29}$$

$$L_3 \equiv [E(T_3, 1) - E(T_1, R_1)] \ . \tag{30}$$

Note that $L_3 = (1-r)L_i$ plus a small sensible heat correction. We are not storing water on the surface in melt pools, so everything melted at the surface is assumed to flow into the ocean ($W_{ro} = W_{ai}$).

Inside the ice there are brine pockets in which there is salt water at the *in situ* freezing temperature. It is assumed that the ice has a uniform overall salinity of S_i and that the freezing temperature is a linear function of salinity. The brine fraction r is given by

$$r = \frac{S_i m}{T_1} .$$

The enthalpy of the combined ice/brine system is given by

$$E(T, r) = r(L_i + C_{po}T) + (1 - r)C_{pi}T . \tag{31}$$

Substituting in for r and differentiating gives:

$$\frac{\partial E}{\partial T} = -\frac{S_i m L_i}{T_1^2} + C_{pi} . \tag{32}$$

Inside the snow, we have

$$Q_s = \frac{k_s}{h_s}(T_2 - T_3) . \tag{33}$$

The heat conduction in the upper part of the ice layer is

$$Q_{I2} = \frac{2k_i}{h_i}(T_1 - T_2) . \tag{34}$$

These can be set equal to each other to solve for T_2

$$T_2 = \frac{T_3 + C_k T_1}{1 + C_k} \tag{35}$$

where

$$C_k \equiv \frac{2k_i h_s}{h_i k_s} .$$

Substituting into (34), we get:

$$Q_s = Q_{I2} = \frac{2k_i}{h_i}\frac{(T_1 - T_3)}{(1 + C_k)} . \tag{36}$$

Note that in the absence of snow, C_k becomes zero and we recover the formula for the no-snow case in which $T_3 = T_2$.

At the bottom of the ice, we have

$$Q_{I0} = \frac{2k_i}{h_i}(T_0 - T_1) . \tag{37}$$

The difference between Q_{I0} and Q_{I2} goes into the enthalpy of the ice:

$$\rho_i h_i \left[\frac{\partial E}{\partial t} + \vec{v} \cdot \nabla E\right] = Q_{I0} - Q_{I2} . \tag{38}$$

We can use the chain rule to obtain an equation for timestepping T_1:

$$\rho_i h_i \frac{\partial E}{\partial T}\left[\frac{\partial T_1}{\partial t} + \vec{v} \cdot \nabla T_1\right] = Q_{I0} - Q_{I2} \tag{39}$$

where

$$\begin{aligned} Q_{I0} - Q_{I2} &= \frac{2k_i}{h_i}\left[(T_0 - T_1) - \frac{(T_1 - T_3)}{1 + C_k}\right] \\ &= \frac{2k_i}{h_i}\left[(T_0 + \frac{T_3 - (2 + C_k)T_1}{1 + C_k}\right] . \end{aligned}$$

Variable	Value (if constant)	Definition
b	3.0	factor
k	0.4	von Karman's constant
ν	$1.8 \times 10^{-6} m^2 s^{-1}$	kinematic viscosity of seawater
Pr	13.0	molecular Prandtl number
P_{rt}	0.85	turbulent Prandtl number
$\dot{\mathrm{E}}$		evaporation
$\dot{\mathrm{P}}$		precipitation
S_0		surface salinity
τ_{io}		stress on the ocean from the ice
τ_{ao}		stress on the ocean from the wind
T		internal ocean temperature
u_τ		friction velocity $\lvert\tau_{io}\rvert^{1/2}\rho_o^{-1/2}$
z_0		roughness parameter

Table 5: Ocean surface variables

2.3 Ocean surface boundary conditions

In the presence of sea ice, the ocean receives surface stresses from both the atmosphere and the ice, according to the ice concentration:

$$K_m \frac{\partial u_w}{\partial z} = \frac{A}{\rho_o} \tau_{io}^x + \frac{1-A}{\rho_o} \tau_{ao}^x \tag{40}$$

$$K_m \frac{\partial v_w}{\partial z} = \frac{A}{\rho_o} \tau_{io}^y + \frac{1-A}{\rho_o} \tau_{ao}^y \tag{41}$$

where the relevant variables are described in table 5.

The surface ocean is assumed to be at the freezing temperature for the surface salinity ($T_0 = mS$) where we use the salinity from the uppermost model point at $z = -\frac{1}{2}\Delta z$. From this, we can obtain a vertical temperature gradient for the upper ocean to use in the heat flux formula:

$$\frac{F_T}{\rho_o C_p w} = -C_{T_z}(T_0 - T) \qquad z \to 0 \tag{42}$$

where

$$C_{T_z} = \frac{u_\tau}{P_{rt} k^{-1} \ln(-z/z_0) + B_T} \tag{43}$$

$$B_T = b \left(\frac{z_0 u_\tau}{\nu} \right)^{1/2} Pr^{2/3} \, . \tag{44}$$

Once we have a value for F_T, we can use it to find the ice growth rates:

$$W_{io} = \frac{1}{\rho_o L_o}(Q_{io} - F_T) \tag{45}$$

$$W_{ao} = \frac{1}{\rho_o L_o}(Q_{ao} - F_T) \tag{46}$$

$$\tag{47}$$

where

$$L_o \equiv [E(T_0, 1) - E(T_1, r_1)] \, . \tag{48}$$

The ocean model receives the following heat and salt fluxes:

$$F_T = AQ_{io} + (1-A)Q_{ao} - W_o L_o \tag{49}$$

$$F_S = (W_o - AW_{ro})(S_i - S_0) + (1-A)S_o(\dot{\mathrm{P}} - \dot{\mathrm{E}})W_o \equiv AW_{io} + (1-A)W_{ao} \tag{50}$$

Variable	Value (if constant)	Definition
C_{pi}	1994 J kg^{-1} K^{-1}	specific heat of ice
C_{pw}	3987 J kg^{-1} K^{-1}	specific heat of water
γ	m_i/m_{w_2}	fraction of water that froze
L	3.16e5 J kg^{-1}	latent heat of fusion
m	-0.0543	constant in freezing equation
n	7.59×10^{-4}	constant in freezing equation
m_i		mass of ice formed
m_{w_1}		mass of water before freezing
m_{w_2}		mass of water after freezing
S_1		salinity before freezing
S_2		salinity after freezing
T_1		temperature before freezing
T_2		temperature after freezing

Table 6: Frazil ice variables

2.4 Frazil ice formation

Following Steele et al. [50], we check to see if any of the ocean temperatures are below freezing at the end of each timestep. If so, frazil ice is assumed to form, changing the local temperature and salinity. The ice that forms is assumed to instantly float up to the surface and add to the ice layer there. We assume balances in the mass, heat, and salt before and after the ice is formed:

$$m_{w_1} = m_{w_2} + m_i \tag{51}$$

$$m_{w_1}(C_{pw}T_1 + L) = m_{w_2}(C_{pw}T_2 + L) + m_i C_{pi} T_2 \tag{52}$$

$$m_{w_1} S_1 = m_{w_2} S_2 \ . \tag{53}$$

The variables are defined in Table 6. Defining $\gamma = m_i/m_{w_2}$ and dropping terms of order γ^2 leads to:

$$T_2 = T_1 + \gamma \left[\frac{L}{C_{pw}} + T_1 \left(1 - \frac{C_{pi}}{C_{pw}} \right) \right] \tag{54}$$

$$S_2 = S_1(1 + \gamma) \ . \tag{55}$$

We also want the final temperature and salinity to be on the freezing line, which we approximate as:

$$T_f = mS + nz \ . \tag{56}$$

We can then solve for γ:

$$\gamma = \frac{-T_1 + mS_1 + nz}{\frac{L}{C_{pw}} + T_1 \left(1 - \frac{C_{pi}}{C_{pw}} \right) - mS_1} \ . \tag{57}$$

The ocean is checked at each depth k and at each timestep for supercooling. If the water is below freezing, the temperature and salinity are adjusted as in equations (54) and (55) and the ice above is thickened by the amount:

$$\Delta h = \gamma_k \Delta z_k \frac{\rho_w}{\rho_i} \ . \tag{58}$$

2.5 Horizontal boundary condition issues

Initial conditions at all points, and ice velocities at the boundaries thereafter, are required to initiate the integration of the system of equations forward in time. The most natural boundary condition

is to take the ice velocity to be zero on the boundaries. This can be done either at a land boundary or at an ocean location where there is no ice. Note that the boundary condition does not affect the ice motion in such circumstances since in the absence of ice the strength is zero. More generally, as long as the ocean boundaries are removed from the ice edge, the coupled nature of the model will cause a natural ice edge boundary condition to be created. However, it is also possible to form an "open" boundary condition by setting the strength equal to zero near a boundary. These gridboxes are called "outflow cells" in Hibler [27]. In the simulation described below, these outflow cells are used at the open edge near Greenland. The primary characteristic of the outflow cells is that the ice strength goes to zero there. The values of P, ζ, and η are all set to zero in outflow cells.

The boundary conditions on the momentum equations are to set u and v to zero at all boundaries, including islands. The ice and snow thickness and ice concentration equations have no-flux boundary conditions imposed along the mask boundaries. The outflow cells contain a radiation condition if the velocity is outward and no change if the velocity is inwardly directed.

3 TOVS Polar Pathfinder Dataset (Path-P)

The NASA/NOAA TOVS Polar (Arctic) Pathfinder (so-called Path-P) data set (Francis and Schweiger [20]) contains fields of atmospheric and surface properties for 20 years extending from 1979 to 1998. The TIROS Operational Vertical Sounder (TOVS) has flown on NOAA polar-orbiting satellites since late 1978 and has generated one of the longest and most complete satellite data records in existence. To generate Path-P, the 20-year global TOVS dataset was subsetted for the Arctic region north of $60°N$, then the radiances were processed with a version of the Improved Initialization Inversion algorithm (Chedin *et al.* [13], Scott *et al.* [47]) that was recently modified to enhance accuracy over snow- and ice-covered surfaces (Francis [19]). Orbital retrievals were averaged in space to $(100\ km)^2$ grid boxes and in time to produce one Arctic-wide field per 24-hour period centered on 12 UTC. The spatial grid is the same as that used for polar passive microwave products and other Arctic dataets (the Equal-Area SSM/I Earth (EASE) grid) and files are presented in the Hierarchical Data Format (HDF).

3.1 Validation

The products contained in the Path-P dataset include atmospheric temperature and moisture profiles, surface skin temperature, cloud amount and height, a variety of boundary-layer parameters, and sea-level pressure (extracted and regridded from NCEP Reanalyses). Path-P temperature and moisture profiles have been extensively and successfully validated with several years of radiosonde data from Russian "NP" ice stations (Schweiger *et al.* [46], Francis and Schweiger [20]).

We illustrate these validation efforts with comparisons of selected Path-P temperature levels (surface, 500 and 900 hPa) and the total precipitable water vapor retrieval (Fig. 4–7). The RMS errors in retrieved upper-level temperatures generally decrease with height and are less than 3 C, except near the tropopause where they increase to about 4 C. Biases are less than 1.5 C at all levels, and are generally slightly negative (retrievals too cold) in the upper troposphere and slightly positive in the lower troposphere. In Fig. 4, we compare Path-P skin temperature values to observed 2-meter air temperatures, which are typically within 2 C of each other except during extended clear-sky calms, which are rare. Retrieved skin temperatures agree surprisingly well with observed 2-meter air temperatures, particularly given that clouds may interfere with surface temperature retrievals. We know of no other surface temperature fields with this time and space resolution that have better accuracy in the Arctic. The comparison of retrieved total precipitable water vapor to rawinsonde values is also encouraging (Fig. 7). The computed errors within each of the five Path-P layers – which are bounded by the pressure levels: surface, 850, 700, 500, 400, and 300 hPa – are comparable with those estimated for the rawinsonde measurements themselves in these extremely cold temperatures, and errors in nearly all layers and in all seasons are well below the corresponding natural variability.

3.2 Interannual variations in surface forcing

Among the variables contained within the Path-P dataset are several which directly enter the surface boundary conditions for the ocean and sea ice, and which presumably control to a large degree their evolution. Of particular importance are sea level pressure (SLP), which dictates the direction and magnitude of surface winds and hence surface stress, and surface air temperature (SAT), which enters importantly into the surface heat budget.

Figures 8–13 show the time-mean and year-by-year average fields of SLP and SAT for the months of March and September. The former month is chosen as typical of late winter conditions; the latter, as noted above, has been shown to demonstrate the greatest interannual variations in sea ice properties. To get an idea of the magnitude of the variations between independent atmospheric

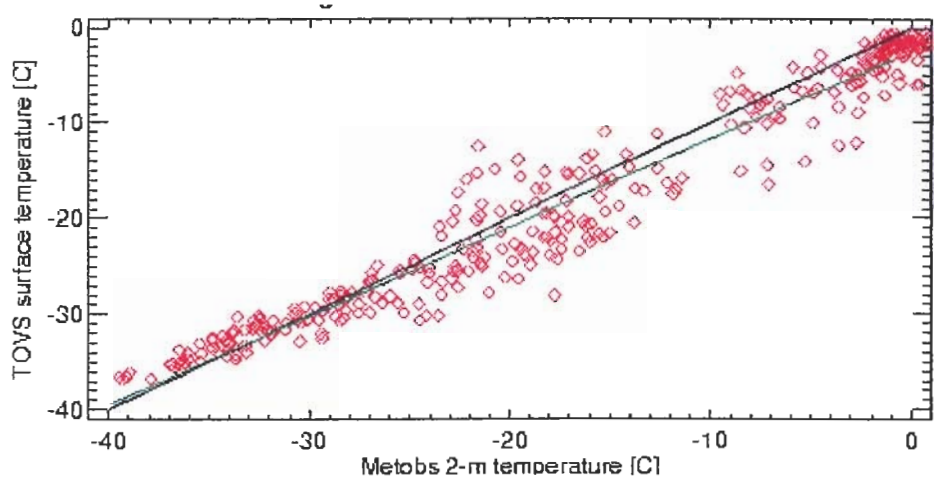

Figure 4: Surface temperature: TOVS versus independent observations. The black line shows perfect (1:1) correspondence, while the green line indicates the best least-square fit (RMS error = 2.66 K).

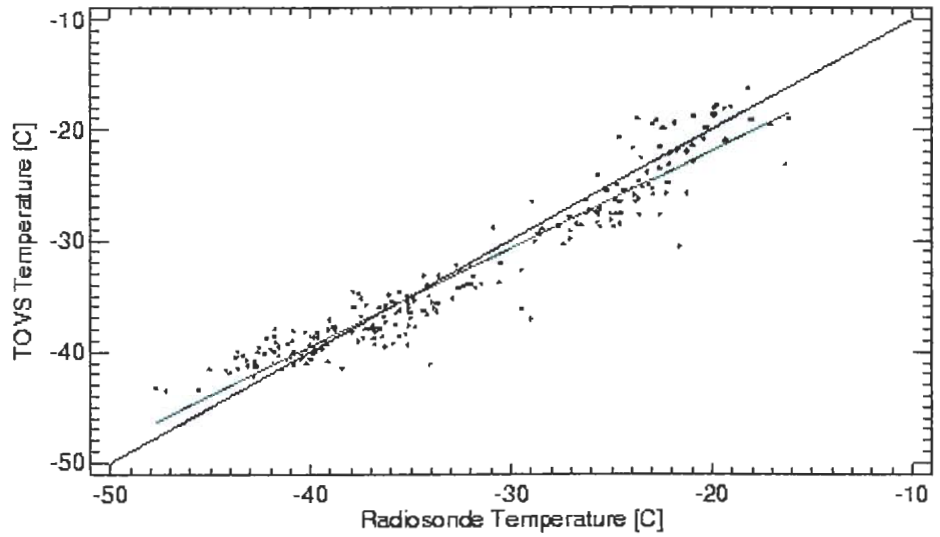

Figure 5: Temperature at 500 hPa: TOVS versus independent observations The black line shows perfect (1:1) correspondence, while the green line indicates the best least-square fit (RMS error = 2.31 K).

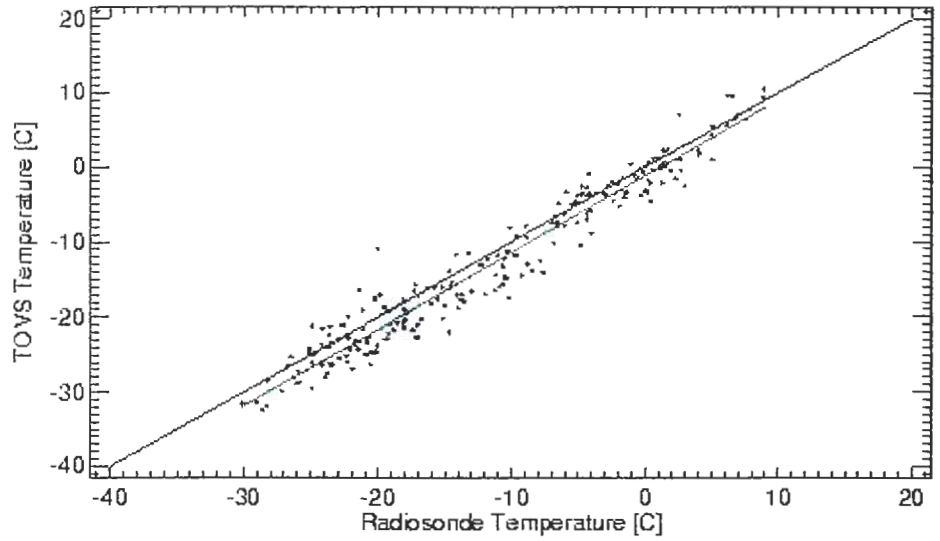

Figure 6: Temperature at 900 hPa: TOVS versus independent observations. The black line shows perfect (1:1) correspondence, while the green line indicates the best least-square fit (RMS error = 2.73 K).

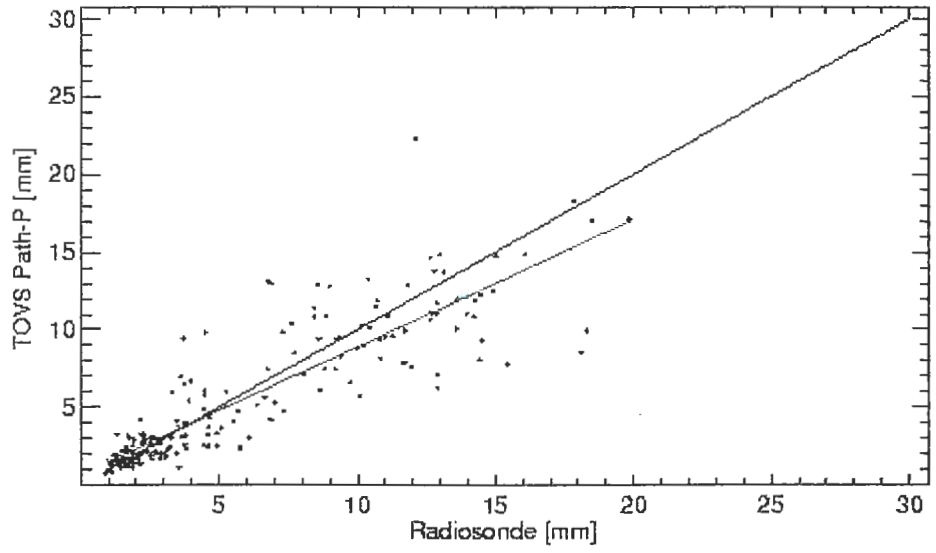

Figure 7: Total precipitable water vapor: TOVS versus independent observations. The black line shows perfect (1:1) correspondence, while the green line indicates the best least-square fit (RMS error = 2.2 mm).

datasets, these figures show both the Path-P SLP (regridded from NCEP reanalyses) and SAT fields, and comparable products produced from Arctic buoy data (Rigor *et al.* [43], [44]). Note that few buoys exist in the eastern Arctic Ocean, and that values obtained there are obtained by interpolating coastal land station data. Thus we expect Path-P values to be more realistic in these areas.

Both the buoy-derived and Path-P datasets show similar time-mean patterns of SLP for late winter and late summer (Fig. 8). In March (Fig. 8a,c), a large-scale SLP gradient of approximately 10 *hPa* occupies the central Arctic, corresponding to weak flow directed from Siberia towards Canada. The SLP gradient in the Western Arctic off Alaska is weak in both datasets. These gradients are further reduced in the September mean (Fig. 8b,d) which shows a weak low pressure cell with about half the pressure contrast seen in March. In both months, the mean fields from the buoy data and from Path-P are highly correlated. (This correlation presumably arises because the NCEP reanalysis – from which the Path-P fields are derived – assimilates the buoy data.) The largest differences between the two datasets occur over Greenland where the Path-P fields show an enhanced high-pressure cell in both months.

In contrast to the rather weak forcing conditions suggested by the time-mean SLP fields, the year-by-year surface pressure fields for March (Fig. 9) and September (Fig. 10) show both much stronger forcing conditions to prevail in many years and much year-to-year variability. For March, well-developed, large-scale flow across the North Pole exists (as it does in the mean) in most years, although the local details of this flow are especially variable in the Western Arctic. Particularly weak basin-scale SLP patterns are seen to occur in 1985, 1991 and 1996, suggesting atypically weak gyre-scale forcing in those years. (We will see what the coupled model has to say on this issue shortly.)

Figure 10 shows the SLP fields for the 15 Septembers from 1982 through 1996. Although on average the month of September was found to have only very weak SLP gradients, the situation in any given September is tremendously variable, with occurrences of strong cyclonic circulation (1983, 1985, 1987, 1988, 1994), strong anti-cyclonic flow (1990, 1996), as well as years with weaker and/or less well organized pressure patterns (1986, 1993, 1995). Note the especially rapid change from strong cyclonic to strong anti-cyclonic circulation between 1988 and 1990, corresponding to the AO regime shift reported by Overland *et al.* [39]. Local SLP gradients – related via geostrophy to the strength of surface winds – are particularly variable in the Western Arctic, suggesting that we should expect similar variability in the strength and direction of sea ice motion over this time period.

Surface air temperature patterns undergo similar large year-to-year variations (Fig. 11–13). As for SLP, maximum variability occurs in September, with much year-to-year change in the Western Arctic. Although the early 1980's seem to suggest a cycle in which warmer- and colder-than-average years occur with equal regularity, the latter half of the 1980's and the 1990's suggest an increasing frequency of warmer-than-average years. September 1995 is the warmest of any of the 15 years. This suggested trend towards warmer September SAT is consistent with the many reports of systematically reduced ice volumes over the past several decades.

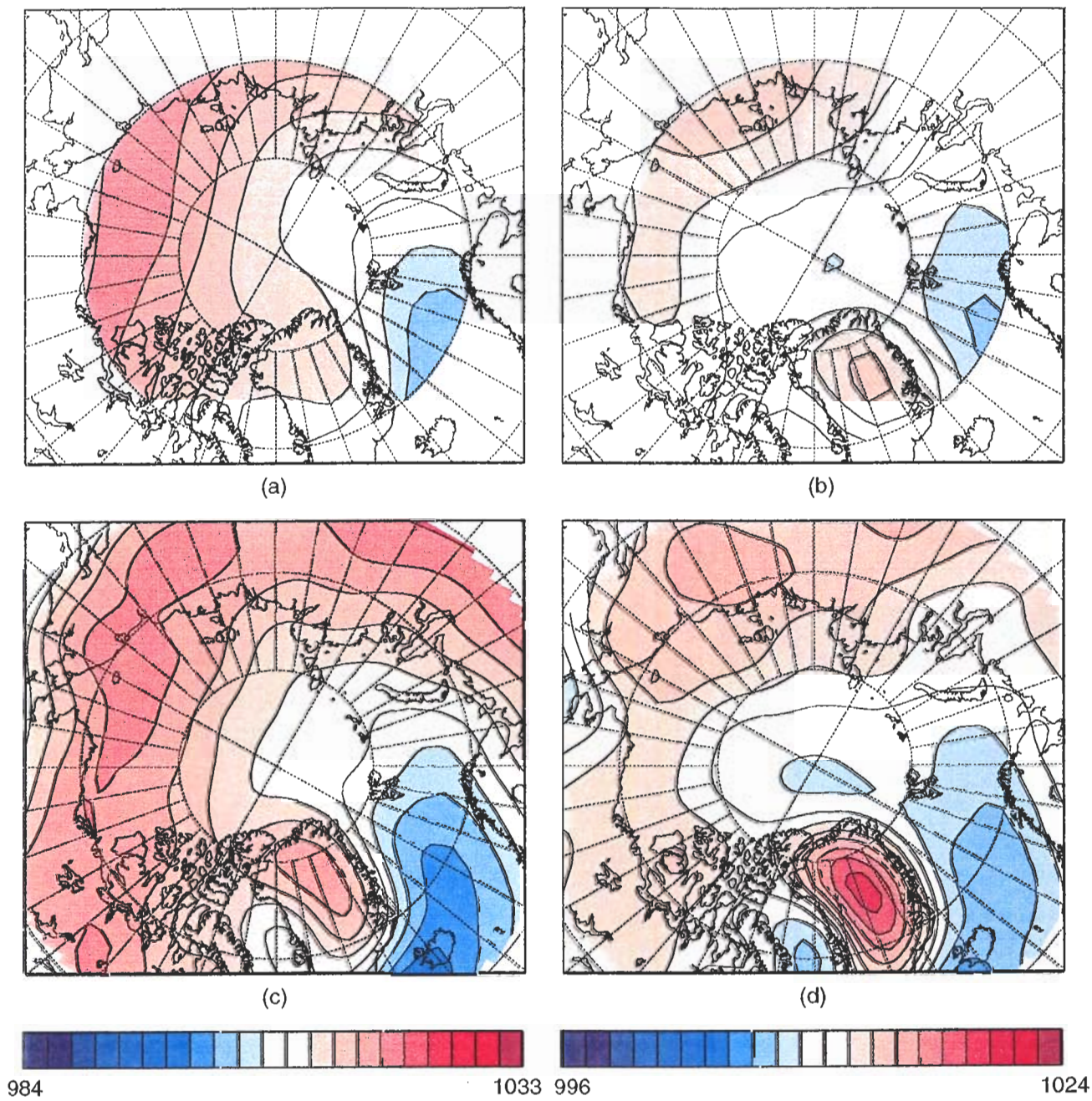

Figure 8: Fifteen-year-average (1982-96) sea level pressure (hPa): (a) March (buoy data), (b) September (buoy data), (c) March (Path-P/NCEP), and (d) September (Path-P/NCEP)

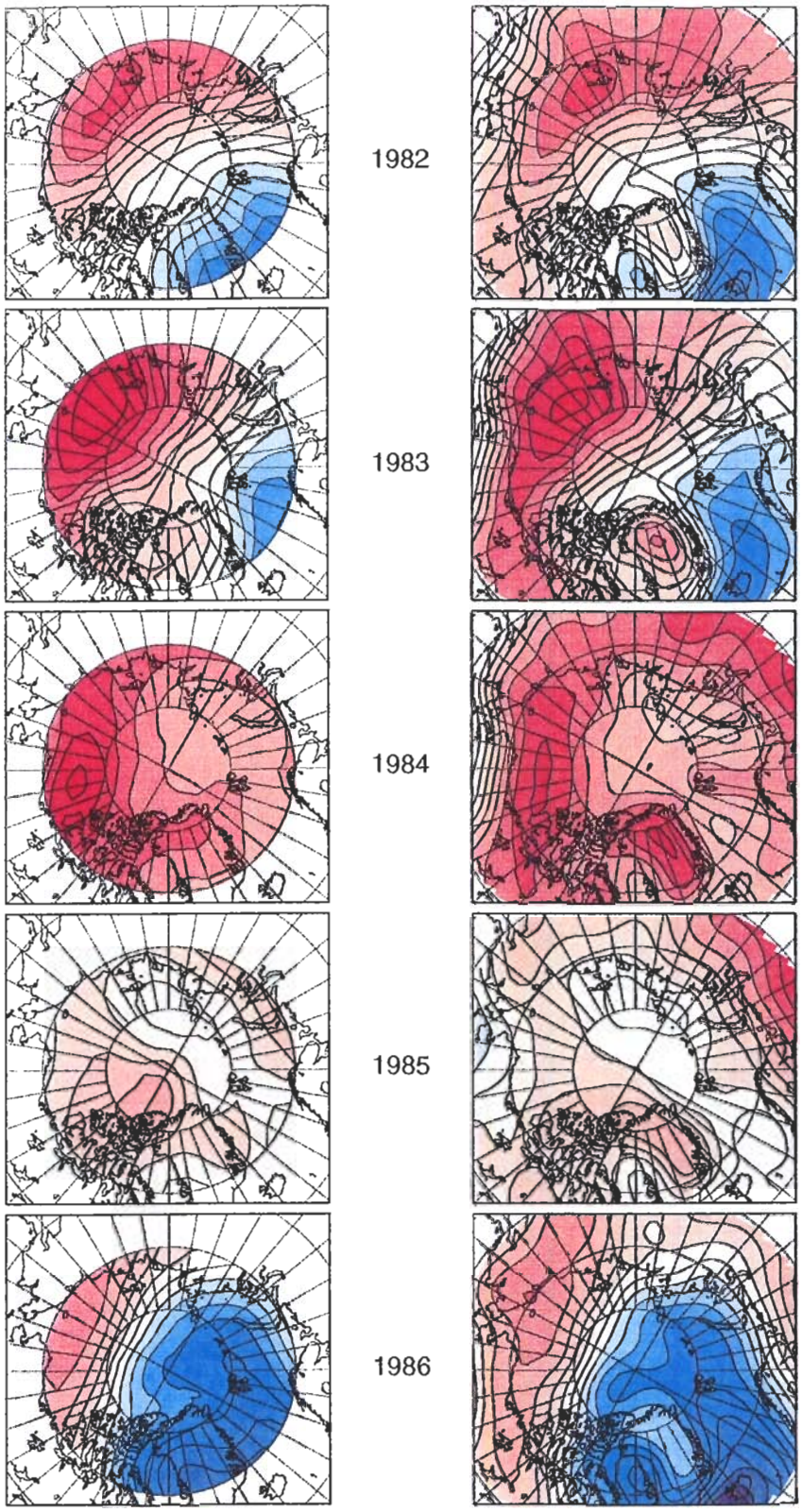

Figure 9: Sea level pressure (hPa) for the month of March (1982 -1996): (left) buoy-derived fields, (right) Path-P fields. The color contours are those used in Fig. 8a,c.

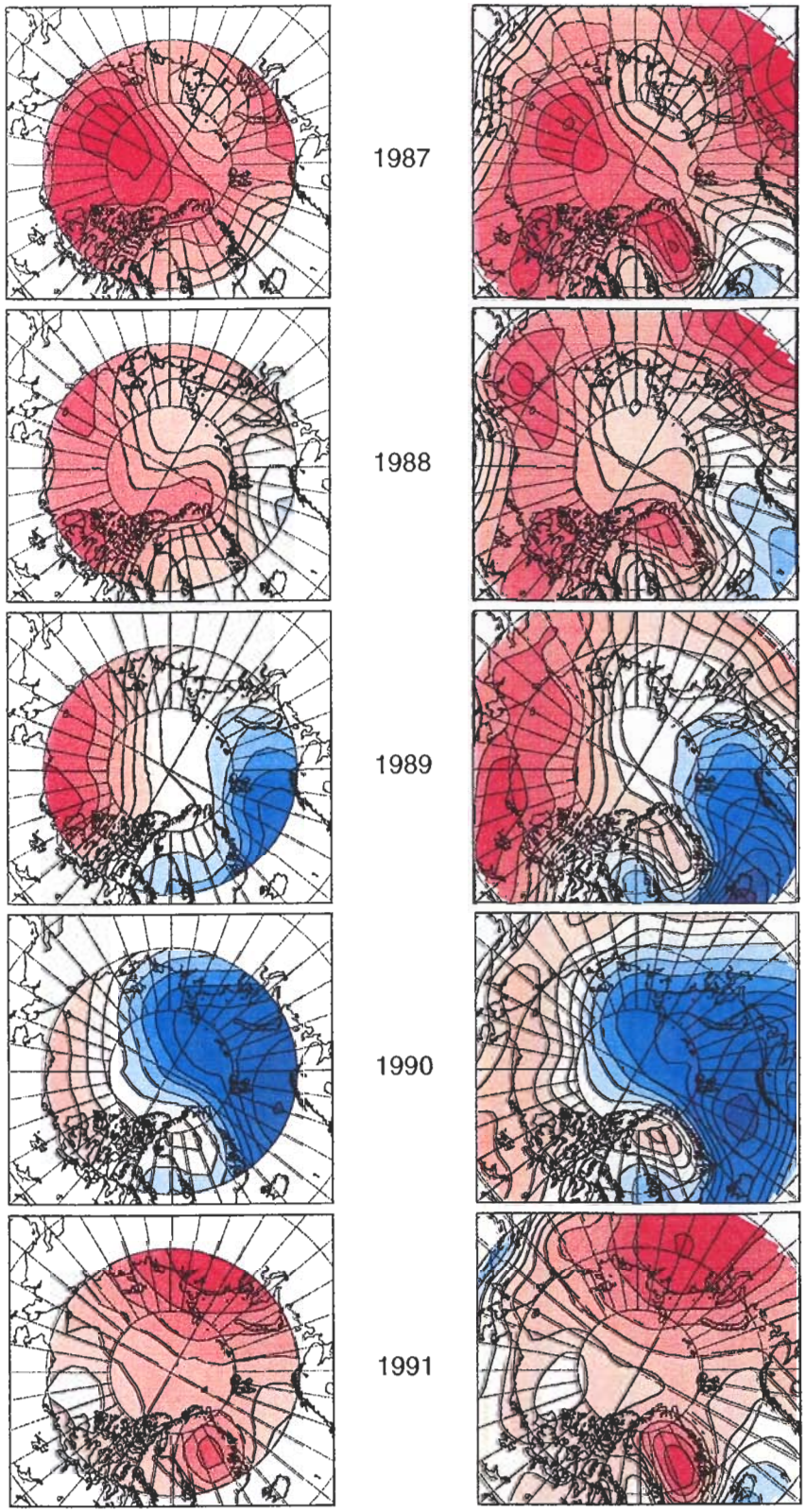

Figure 9 continued.

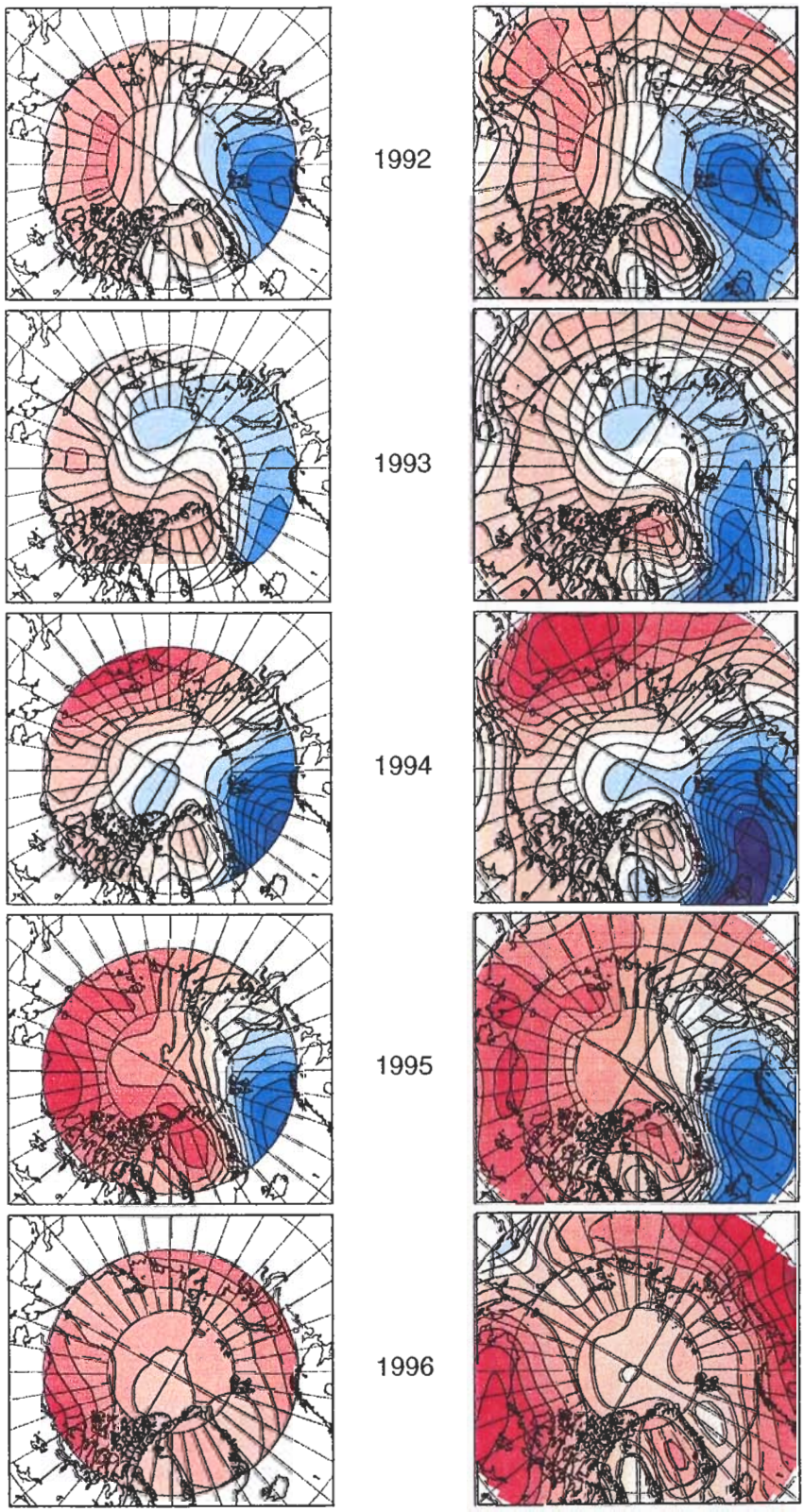

Figure 9 continued.

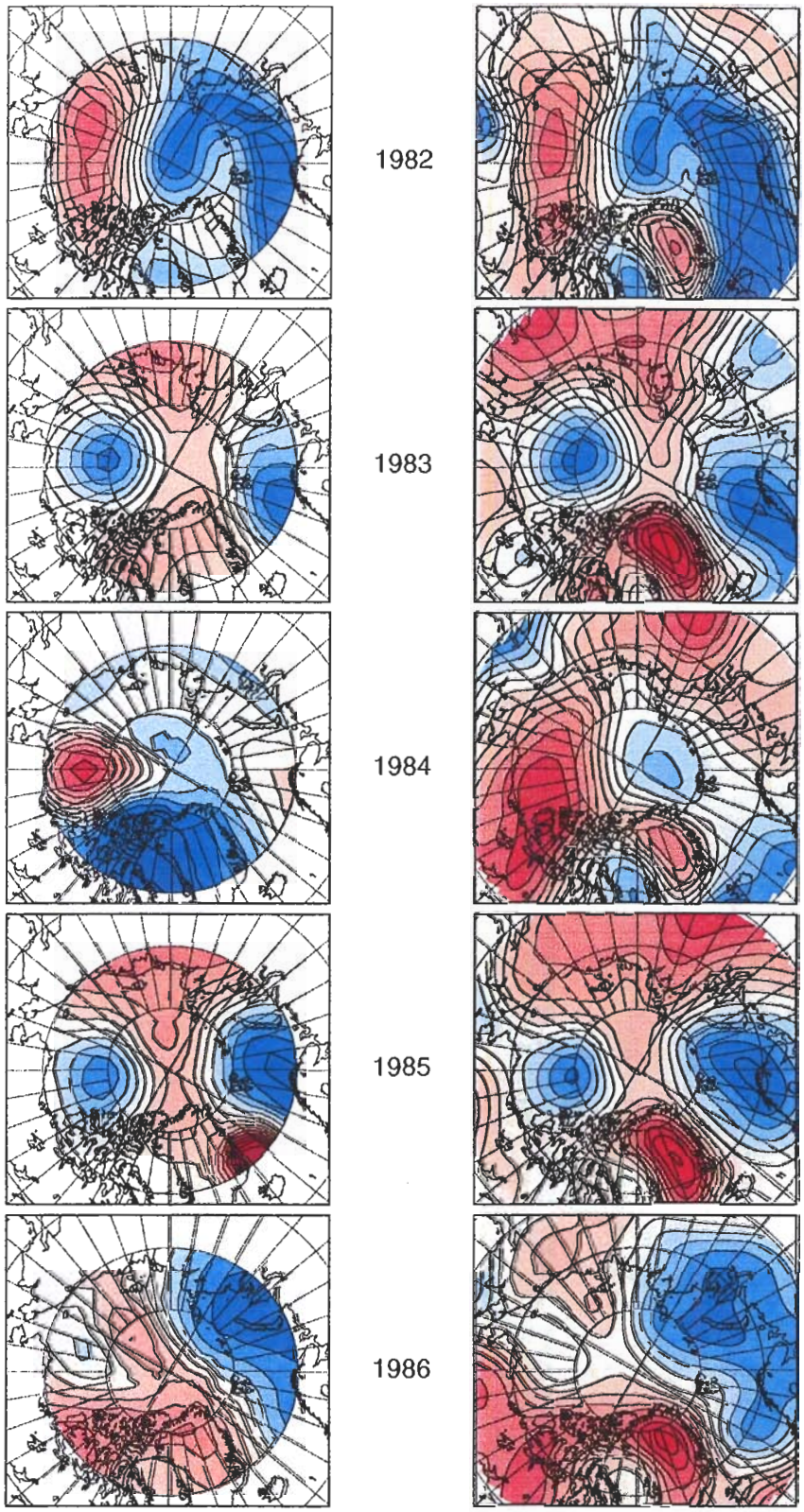

Figure 10: Sea level pressure (hPa) for the month of September (1982–1996): (left) buoy-derived fields, (right) Path-P fields. The color contours are those used in Fig. 8b,d.

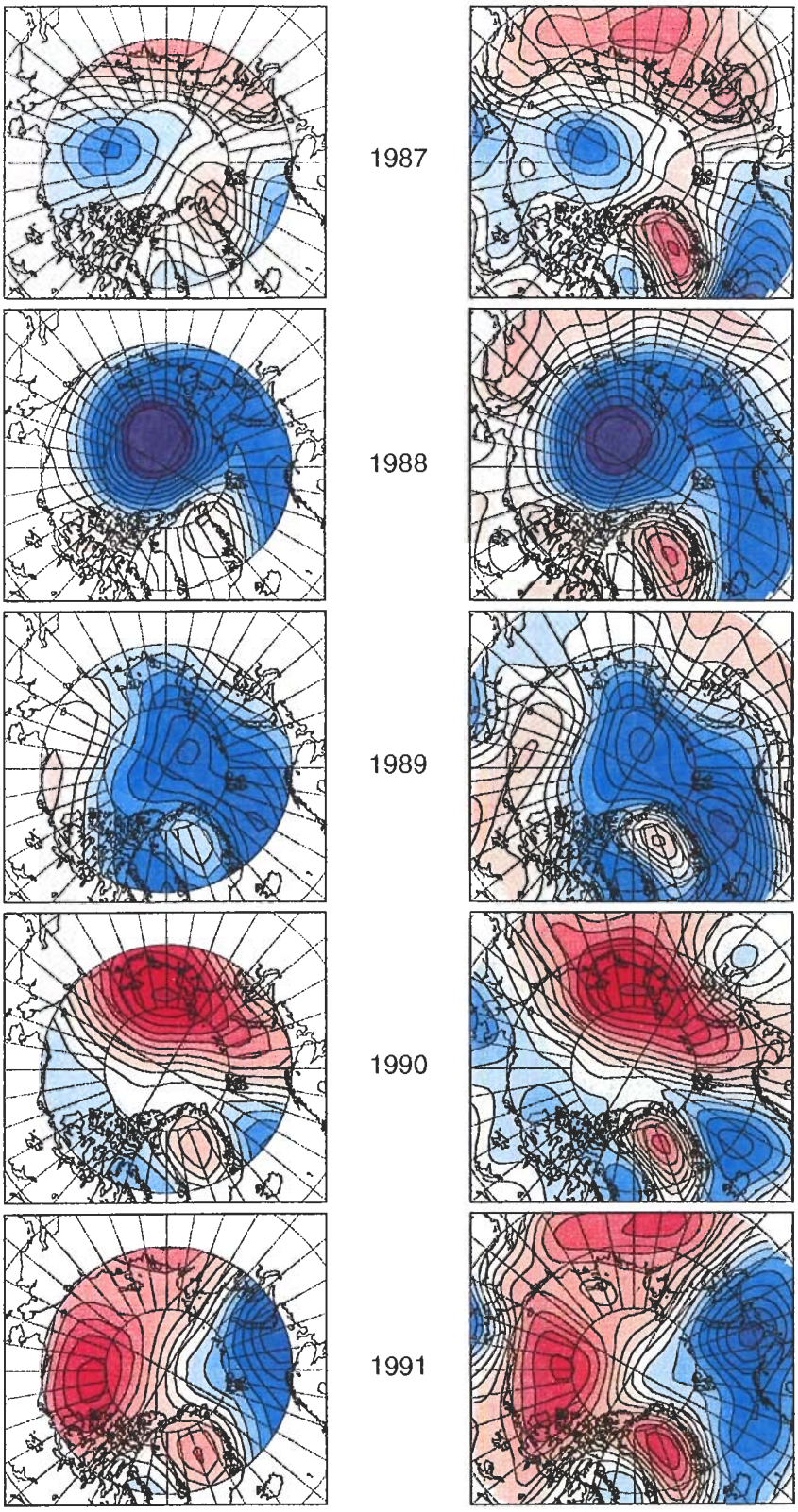

Figure 10 continued.

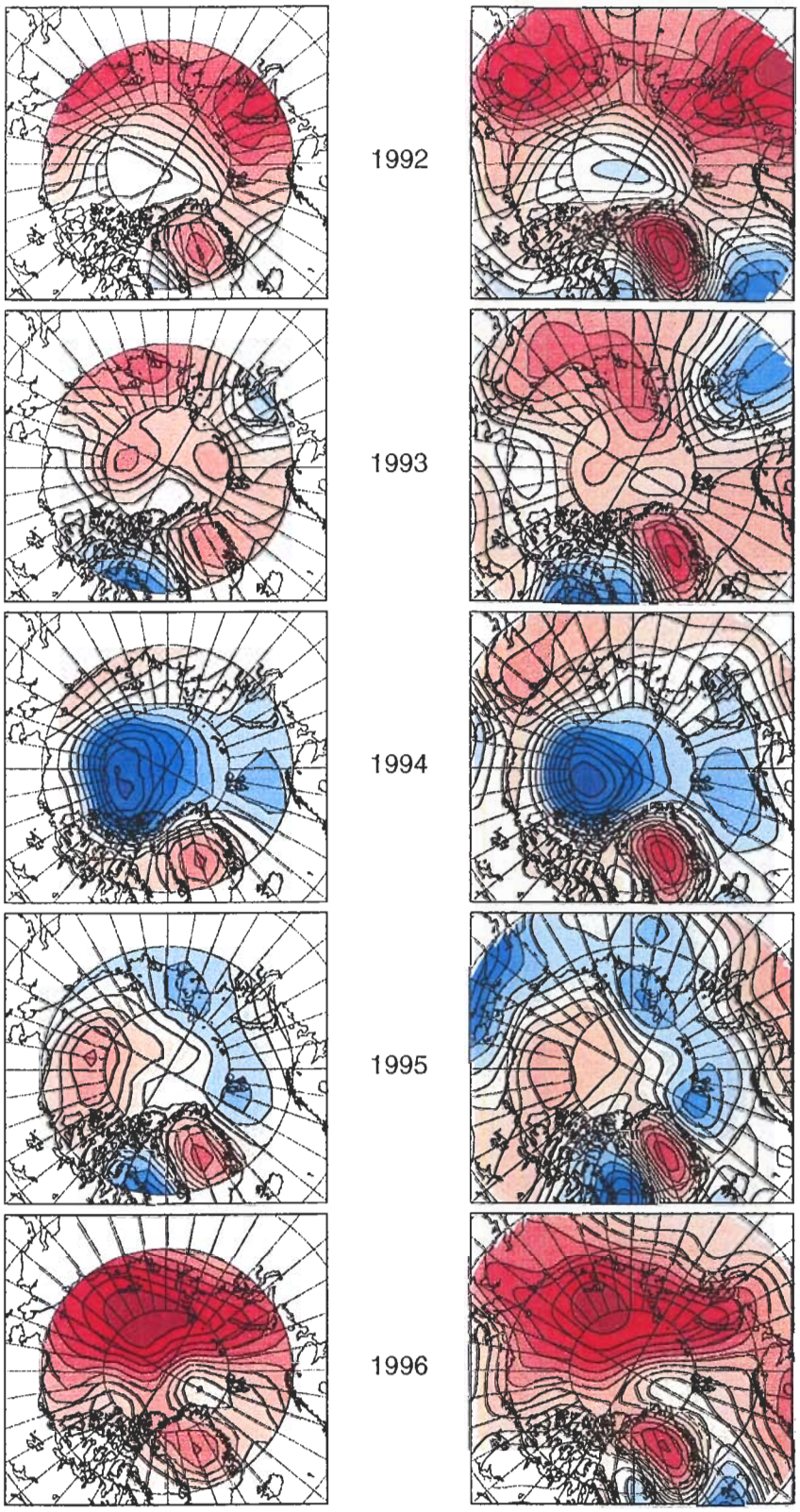

Figure 10 continued.

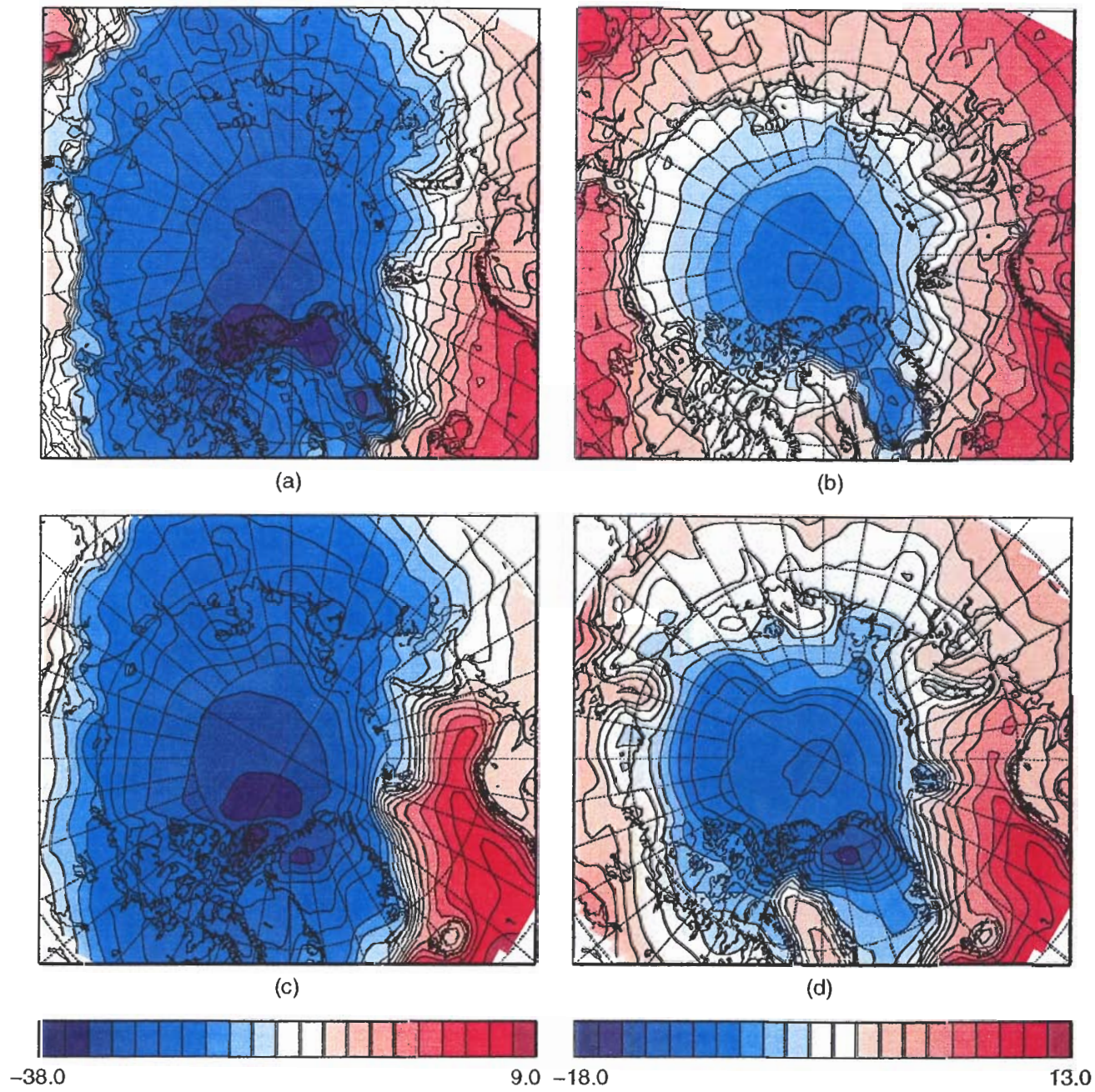

Figure 11: Fifteen-year-average (1982-96) surface air temperature (C): (a) March (buoy data), (b) September (buoy data), (c) March (Path-P), and (d) September (Path-P)

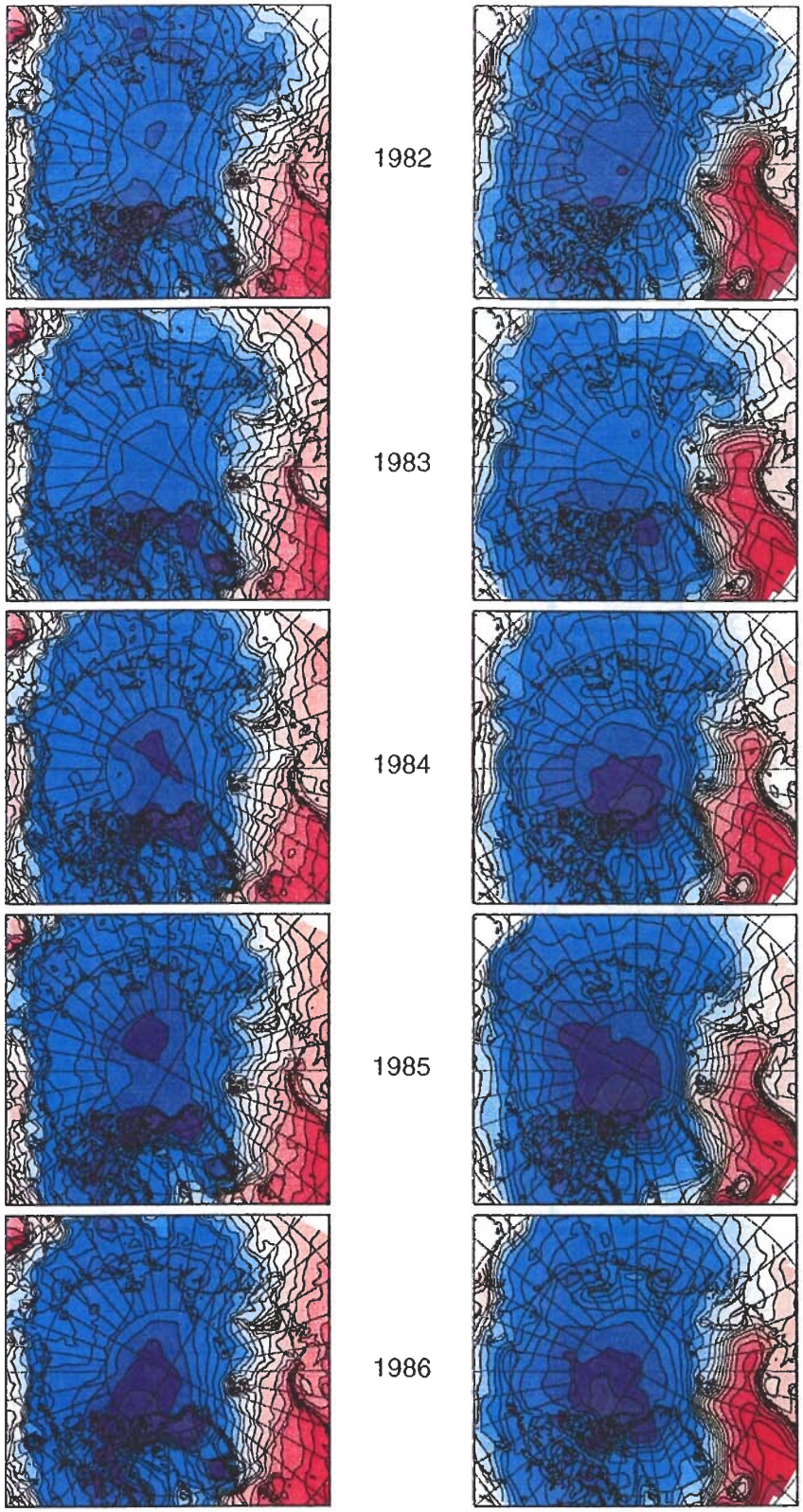

Figure 12: Surface air temperature (C) for the month of March (1982–1996): (left) buoy-derived fields, (right) Path-P fields. The color contours are those used in Fig. 11a,c.

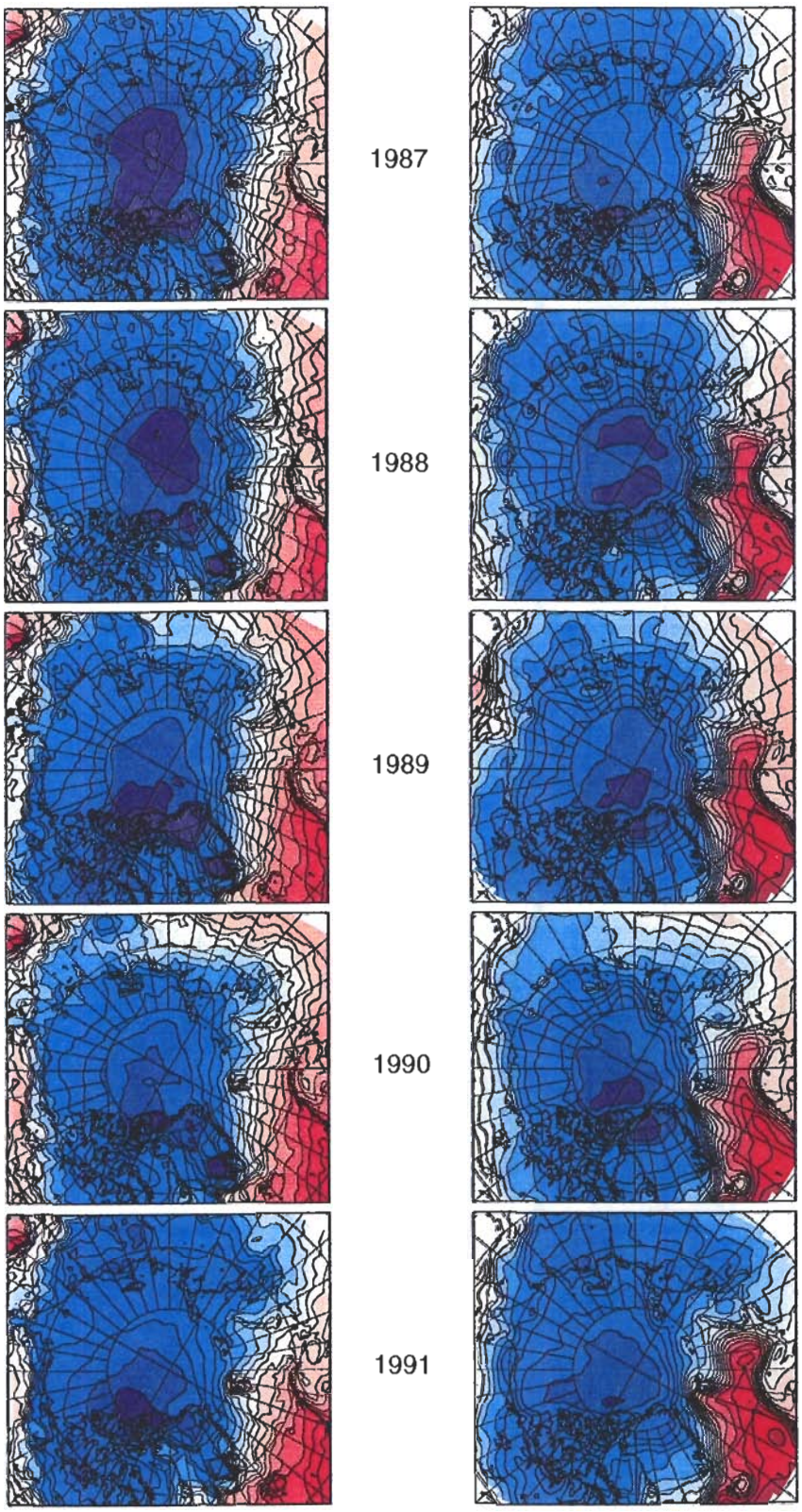

Figure 12 continued.

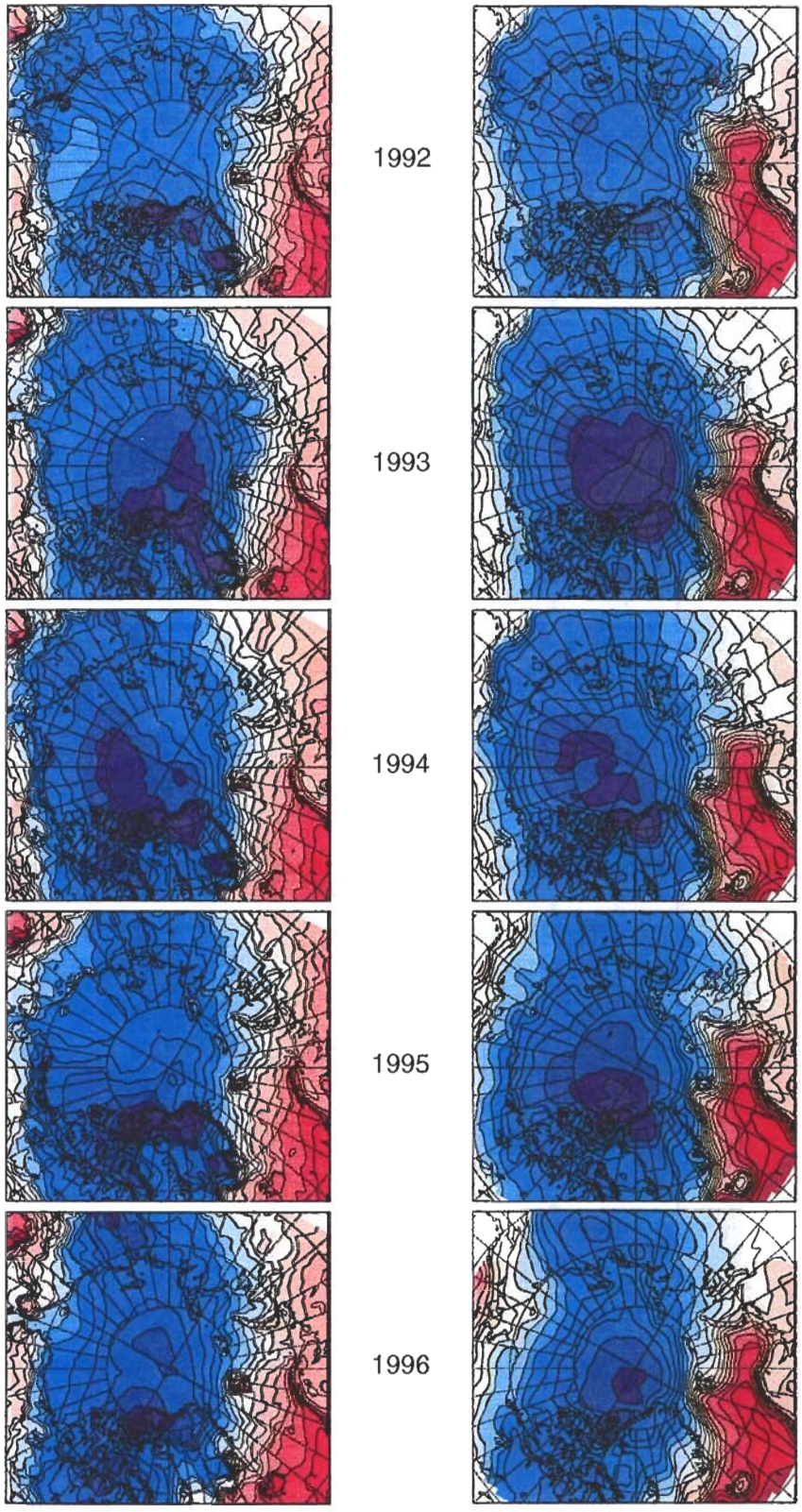

Figure 12 continued.

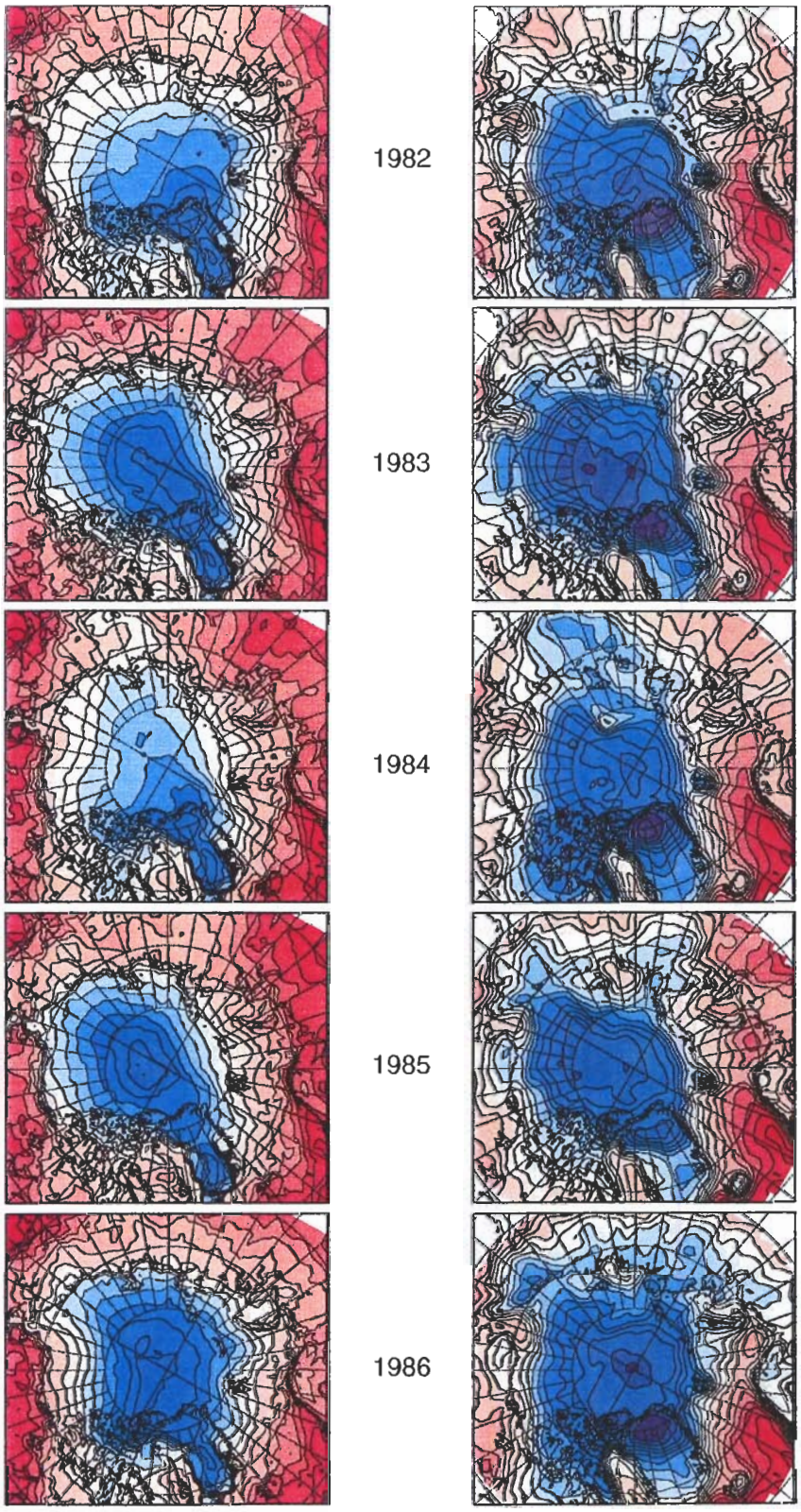

Figure 13: Surface air temperature (C) for the month of September (1982–1996): (left) buoy-derived fields, (right) Path-P fields. The color contours are those used in Fig. 11b,d.

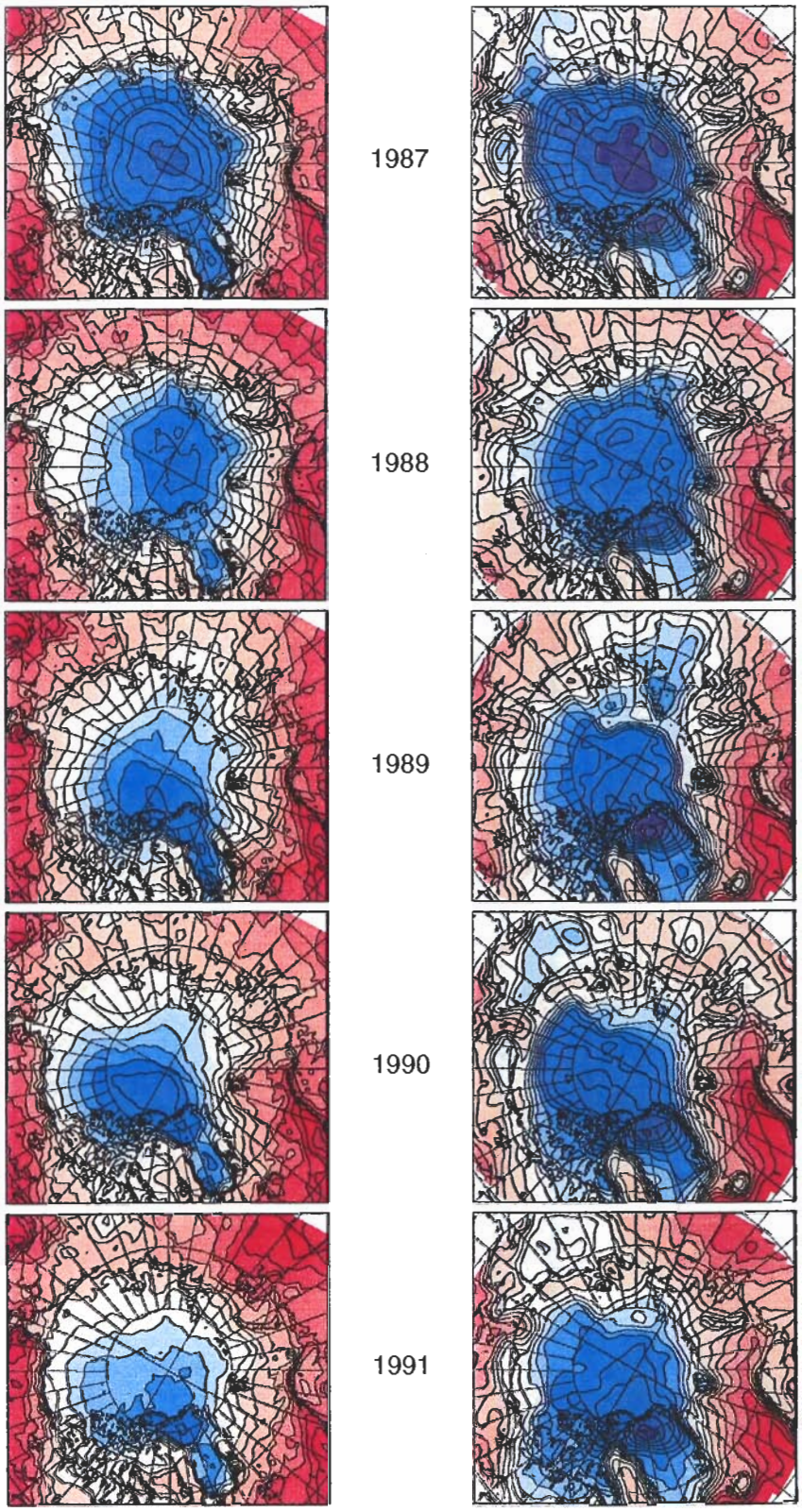

Figure 13 continued.

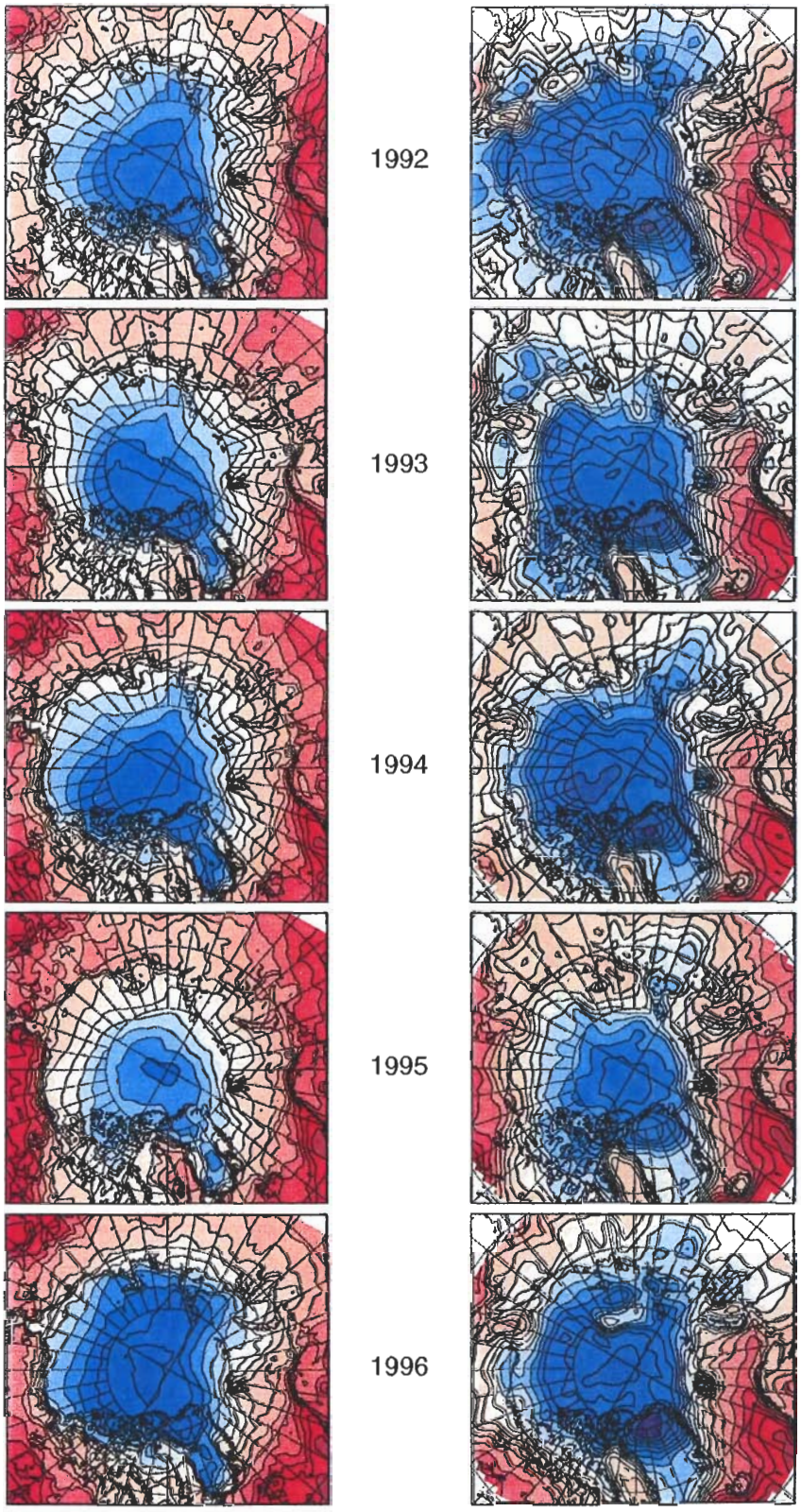

Figure 13 continued.

4 Model configuration and spin-up

The configuration of the coupled model requires: setting up of the model geometry, the initial conditions and the forcing fields, and choosing the mixing parameters and the timestep. Improvements in these areas – relative to our earlier study (Hedström [26]) – include a model geometry that incorporates the entire Arctic Ocean and its full water column depth, and a more complete surface mixing module, as well as the utilization of the improved atmospheric forcing datasets described in §3.

4.1 Model geometry

We built three grids in the same domain, having 64×48, 128×96, and 256×192 horizontal gridpoints. The finest grid, with a resolution of about ten kilometers in the Western Arctic, was computationally unaffordable at the time these computations were carried out (although with advances in parallel computer performance, and using our newest circulation model, higher horizontal and vertical resolution is now feasible). All of our early test runs were done on the coarsest grid, on the SGI PowerChallenge at IMCS. The final multi-year simulation was conducted on the medium-fine grid on the SGI Origin 2000 at the Naval Research Lab, requiring approximately 100 CPU hours per simulated year.

In the earlier study, the ice model dictated the use of a rectangular grid of uniform (20 km) spacing, covering the Western Arctic Ocean only. Since this constraint has now been removed, we are able to construct, and to use, curvilinear grids of varying resolution. Figure 14 shows the medium-fine grid used in the final phase of this study, and the accompanying grid resolution in the two horizontal dimensions. Note that the finest resolution occurs in the Western Arctic, where horizontal grid spacing is at, or less than, 20 km. The curvilinear grid allows some flexibility in spatial distribution of resolution, and in alignment of coordinate lines to follow the local coastline. Nonetheless, masking of islands and some segments of the coastline are necessary, as seen in Fig. 14.

The model bathymetry was determined in several steps. First, the ETOPO5 bathymetry was bilinearly interpolated to the grid (Fig. 15, upper). This was done with the bathtub program in Gridpak (Wilkin and Hedstrom [47]). Second, the bathymetry was clipped to lie between 50 and 5000 m in depth. Finally, the bathymetry was smoothed with a filter designed to reduce the fractional change in depth from one gridpoint to the next, resulting in the bathymetry shown in the lower half of Fig. 15. In the unfiltered bathymetry field, it can be seen that there are places where the depth goes from 100 m to 1000 m between adjacent gridpoints. The vertical sigma coordinate system in the model follows the bottom contours, but this is only sensible when the bathymetry is horizontally resolved by the grid.

4.2 Surface forcing

As discussed above, the Arctic is forced primarily by atmospheric fluxes of momentum, heat and moisture, with additional forcing arising from coastal buoyancy inputs (fresh water runoff) and net exchanges between the Arctic and both the Bering Sea and the Atlantic Ocean. Of these three forcing mechanisms, only the first is incorporated explicitly here. Direct exchanges (mass inflow/outflow) with the Bering Sea and the Atlantic Ocean are not included, although weak nudging bands on the tracer fields are used to crudely approximate the effects of such mass exchanges.

The model is forced at the surface via imposed fluxes of momentum and heat, as described above, using the Path-P atmospheric datasets. The forcing fields are interpolated in time from the daily datasets to the required model timestep, and are bilinearly interpolated in space onto the model grid. Within the model, the wind and water stresses are applied directly to the ice momentum equations. For the water momentum equations, the applied atmospheric and sea ice

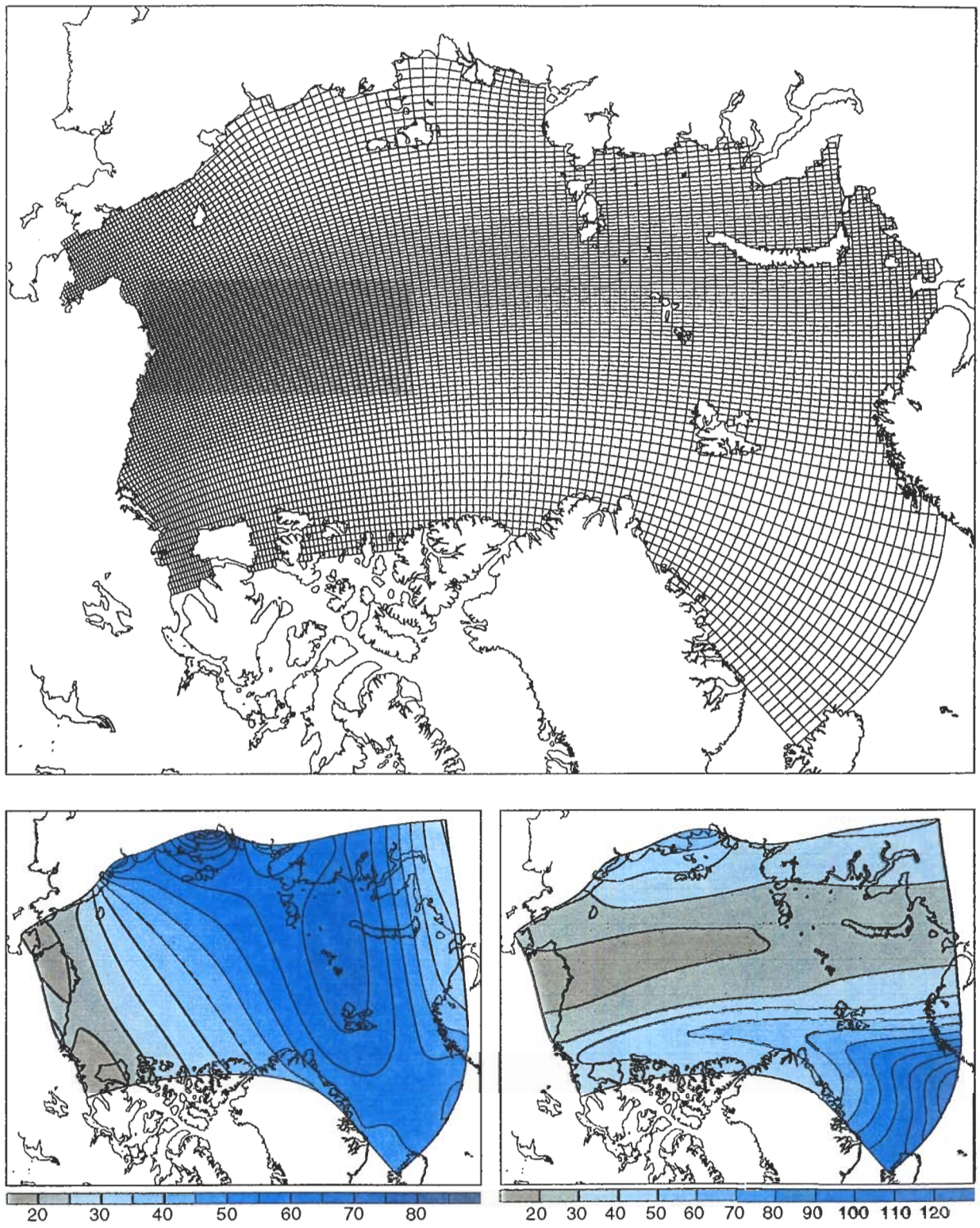

Figure 14: The numerical curvilinear grid used for the simulation. The resulting horizontal grid spacing fields (in km) are shown at the bottom.

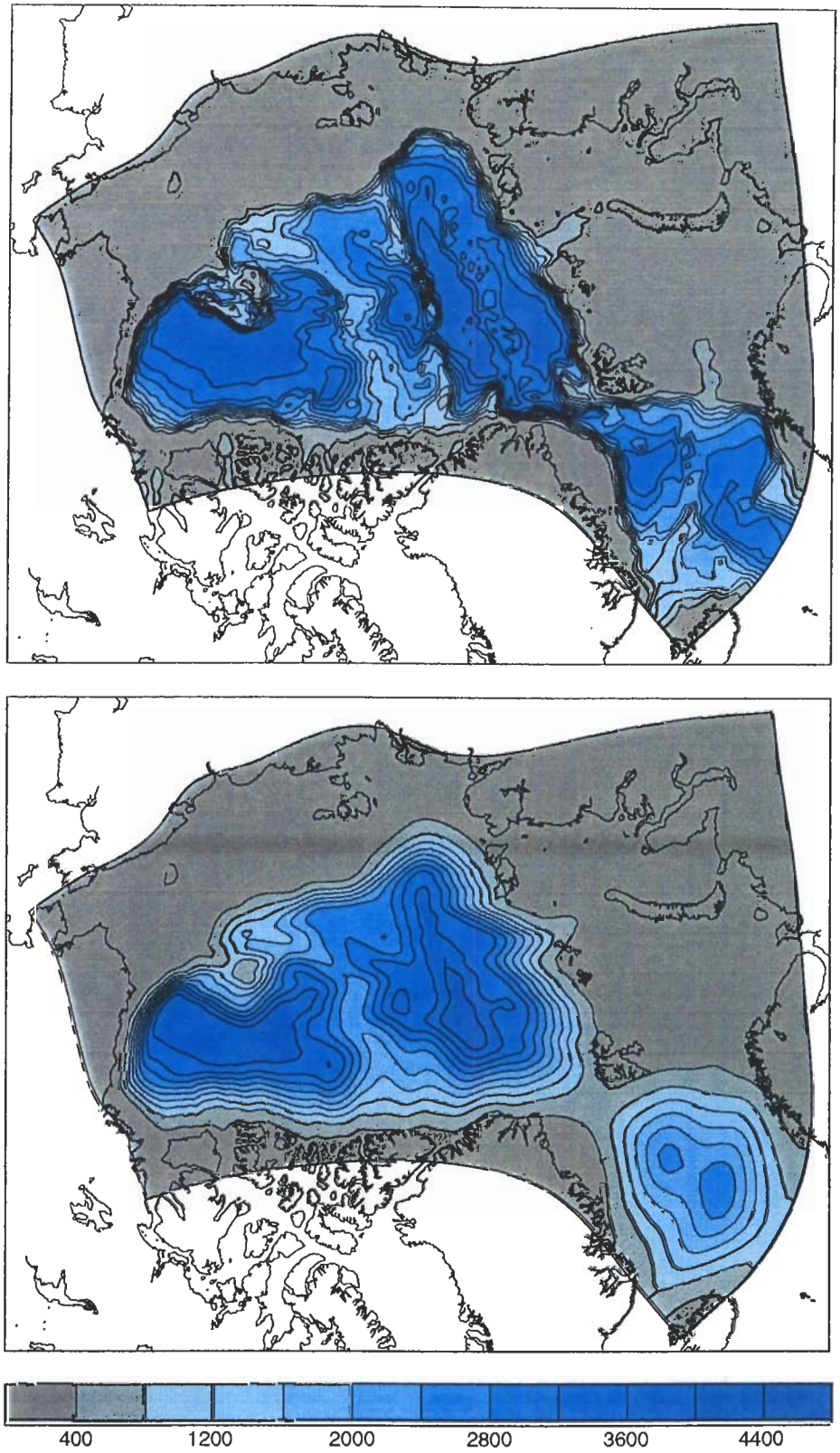

Figure 15: Model bathymetry (km): (upper) original ETOP05 bathymetry, (lower) clipped and smoothed bathymetry.

stresses are weighted as described in §2.3. Within the ocean, vertical mixing rates for momentum and heat are computed using the "K-Profile Parameterization" scheme of Large *et al.* [33].

Lastly, a "nudging" on the temperature and salinity fields is included on the open boundary lying between Greenland and Iceland to restore tracer fields to Levitus climatology with timescales from five to sixty days.

4.3 Viscosity, diffusion, timestep

The ice component of the model has an implicit diffusion through the third-order upwind advection scheme on the ice and snow thickness and the ice concentration. The ice momentum equations also contain smoothing operators with non-linear viscous coefficients. The ocean component, on the other hand, has options for what smoothing to apply and at what strength. We have chosen to use a horizontal Laplacian value of 1000 m^2/s for diffusivity. This value is scaled by grid spacing in such a way that the regions of enhanced resolution in the Western Arctic receive reduced values of this harmonic coefficient. The ocean tracer and momentum fields also have the implicit smoothing provided by the third-order upwind advection scheme. The bottom drag coefficients are given in table 2. The walls are free-slip in the water and in the ice.

Version 2 of the coupled circulation/sea ice model utilizes a split-explicit time stepping scheme in which the depth-integrated component of the circulation – which, in a free surface model, is constrained by the propagation of surface gravity waves – is assigned a shorter timestep than the depth-varying circulation, the tracers and the sea ice. For the simulation reported here, the short and long timesteps are 15 and 300 seconds, respectively.

4.4 Spin-up and early testing

Both the ice and ocean components of the model require initial conditions. The circulation field is assumed to start from rest; that is, the initial ice and ocean velocities are set to zero. The initial ice concentration is set to 1.00 (complete ice cover) since the model was started on January 1. The initial ice thickness is set to a uniform value of 1.65 m, the thickness of 1.5 m of water. This is not a realistic value, but it was assumed that the thickness would reach an equilibrium after several years of integration. Initial conditions for ocean temperature and salinity fields are also required. These were obtained from the Environmental Working Group (EWG) Joint U.S.-Russian Atlas of the Arctic Ocean (winter period; Arctic Climatology Project [54]).

The early tests were used to assess our ability to run with the features required. For instance, we turned on the advection of snow and had to improve the melting of snow – *e.g.*, if ice melts laterally, the snow should also melt laterally. The early changes also brought "hakkis" more in line with the model description in Mellor and Kantha (MK89). The hardest part of the model to adjust turned out to be the treatment of vanishingly thin ice. If it isn't treated in a consistent manner, the marginal ice zone can contain tall thin ice floes. These floes can be covered with tall, thin drifts of snow as well. We adjusted the limiters on ice and snow volume and concentration to obtain sensible results, but the whole business is rather unsatisfactory. One has to set the ice concentration to the minimum when the ice volume gets to its minimum and vice versa. We also had to add other limiters: the brine fraction can't get higher than 20% and the ice temperature solver needed to be kept in bounds. We also solved for the ice temperature iteratively, borrowing ideas from the CICE model (Los Alamos).

We tried both MPDATA and third-order upwind advections schemes, both in the ice and the ocean. Neither scheme allows oscillations in the tracer field such as commonly occurs with second-order centered schemes. The differences between the two schemes was negligible; however, the ice ridging scheme was easier to implement with the third-order upwind advection in the ice.

The Gray and Killworth ice ridging scheme is actually a family of schemes. The user must pick a function for a ridging parameter that depends on the ice concentration. The ridging parameter is fixed at the limits of no ice and complete ice cover, but must be specified for partial ice. We tried two different shapes for this function, but were never quite satisfied with the results. The ridging parameter leads to the ice thickness increasing when the ice is convergent, meaning that ridging takes place before all the leads are closed. The ice pressure is similar in that it provides a force which slows the ice convergence when the fraction of leads becomes small. In future, these two functions should be derived simultaneously so that the resistance to convergence and the amount of ridging that takes place are consistent with each other. In our runs, the ice ridging happened too easily, before the ice pressure turned on, and was therefore disabled in the final simulation.

After a certain amount of experimentation, along the lines indicated, the model reached a sensible seasonal equilibrium cycle. From that point, model integration was continued from the beginning of our atmospheric forcing datasets – that is, from January 1982 – forward in time until the end of 1996. Monthly mean history records of all surface variables (surface ocean and ice) were retained for subsequent analysis.

5 Results and evaluation

5.1 The Beaufort Gyre

As we have mentioned, the principal gyre-scale circulation pattern in the Western Arctic is the Beaufort Gyre, a generally cyclonic circulation that is largely wind-driven. In our prior study (Hedström *et al.* [26]), only the upper water column was actively treated; in a sense, the lower water column was assumed to be unmoving. Here, we have the benefit of capturing the full water column, and, in particular, its participation in the net, top-to-bottom flow field.

Since our history files retain only surface information, we use the model-derived sea surface height field to obtain an estimate of the net barotropic circulation for September in all 15 years. We do so by taking the monthly averaged sea surface height field, by applying the geostrophic approximation to obtain estimates of the barotropic flow field associated with it, and by solving a simple Poisson equation (subject to no flow through the coastal boundaries) to derive an estimate of the streamfunction associated with this the depth-integrated flow. The results of this analysis are shown in Fig. 16.

The long-term-mean streamfunction (Fig. 16, upper left) clearly shows the mean tendency for cyclonic flow covering the Beaufort Basin between the continental shelves and the Lomonosov Ridge. Our estimate for this component of the depth-integrated circulation suggests for September in these years a total circulation of something in excess of 25 Sverdrups. On average, circulation elsewhere in our model is less well organized and much weaker.

As suggested by the interannual variability in surface forcing (§3), net circulation in the Beaufort Gyre is seen to vary by nearly 100% across the 15 years of our simulation. The late 1980's – a period covering the AO regime shift in 1987 – exhibits a particularly weak gyre-scale circulation. Indeed the Beaufort gyre is nearly shut down in 1986 in this model simulation. Following this period, the 1990's once again show a vigorous, sustained, and possibly accelerating, Beaufort circulation. To what extent this robust circulation in the 1990's reflects (and is possibly related to) the retreat of the sea ice we describe further below is unclear.

5.2 Ice concentration

Although available oceanic observations preclude reliable multi-year estimates of net circulation (nearly anywhere) in the Arctic Ocean, we do have basin-wide estimates for many years of ice parameters such as ice concentration and ice motion. Some additional estimates of ice thickness are also becoming available. The best observed of these fields is ice concentration which for many years has been remotely observed from satellites. A summary of these observed fields, as obtained from NSIDC (Cavalieri [12]), along with the corresponding model products, is shown in Fig. 17–19.

The time-mean (1982–1996) sea ice concentration for March and September is shown in Fig. 17. In an average March, as expected, sea ice concentration is 100% nearly everywhere in the Arctic in both observations and in the model hindcast. Although realistic in its sea ice concentration estimates over much of the basin, the model does show two unrealistic features: a tendency for reduced ice concentration near to some coastlines (*e.g.*, the Western Arctic) and too much ice in the extreme Eastern Arctic near the paths of connection to the Atlantic Ocean. These erroneous features are in all likelihood due, in the former case, to the omission in our ice model of "fast ice" which acts to retain ice in regions of shallow water, and in the latter to the particular open boundary condition treatments in use along the edges which communicate with the Atlantic. The introduction of more effective means of exchanging properties with the Atlantic would limit ice concentration in the Eastern Arctic, as is observed.

The mean ice concentration in September is also reproduced by the model with considerable skill (Fig. 17b,d). With the exception of some particular smaller-scale features on the Siberian

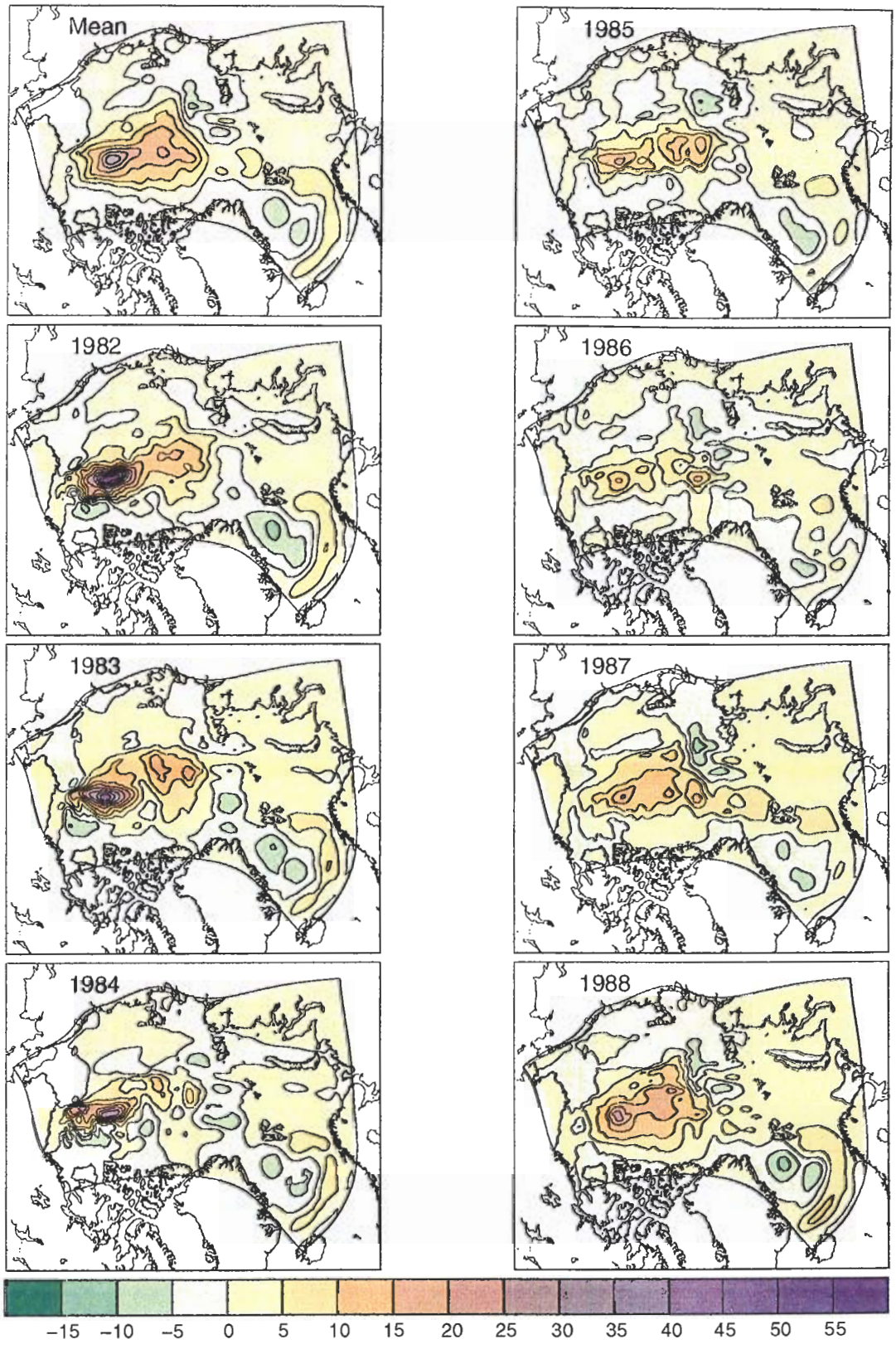

Figure 16: Derived streamfunction (Sv) for September (Mean, 1982-1996)

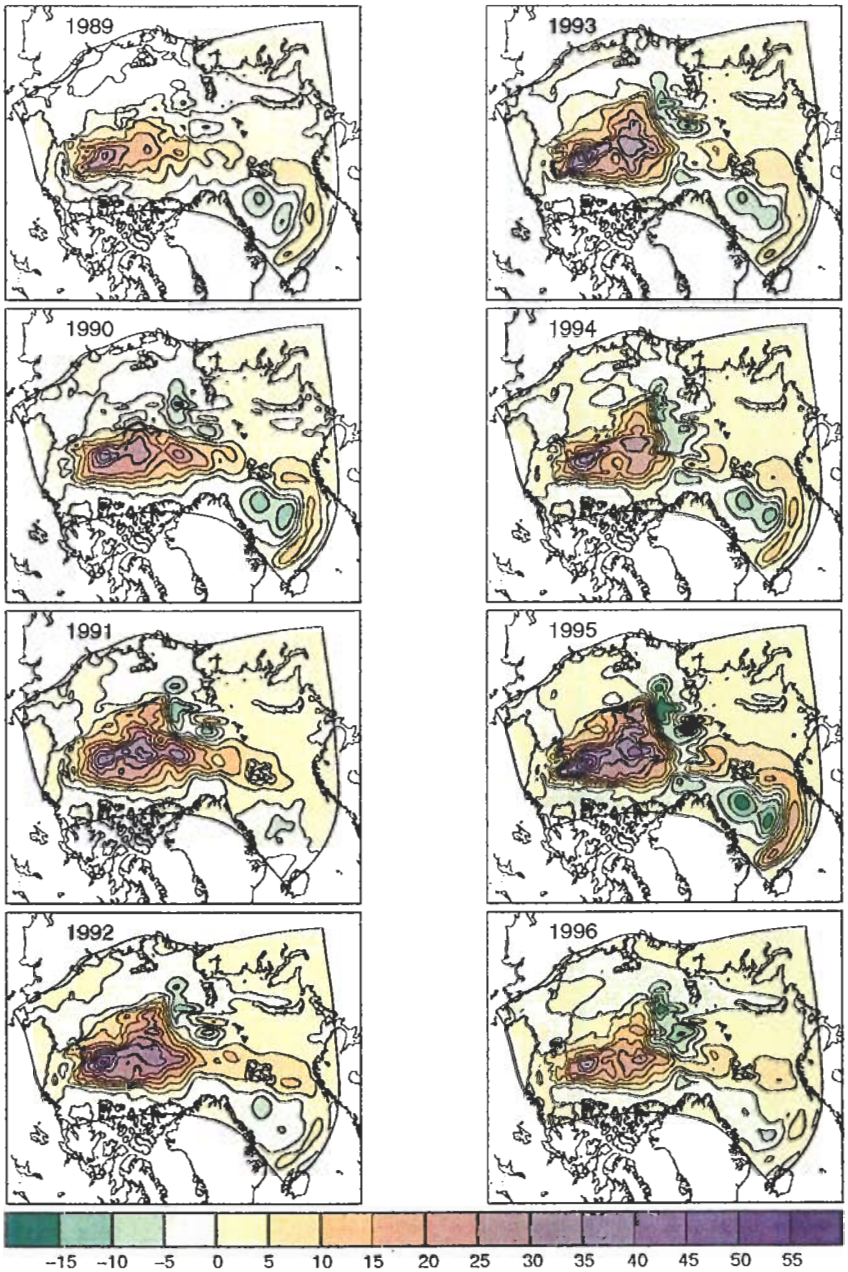

Figure 16 continued.

shelf and in the Beaufort Sea – both involving somewhat too much melt-back in the model – the large-scale features of September mean ice concentration are similar in the observations and the model hindcast.

As our interest is focused primarily on the Western Arctic conditions, it is valuable to narrow our field of view in order to look more closely at the regional mean fields of ice concentration (Fig. 18). As suggested in our description of the gyre-scale mean fields of ice concentration, the patterns in the Western Arctic are well reproduced except for too little ice directly adjacent to land in March (Fig. 18a,c) and for a wedge of excessive melt-back extending outward from the continental shelf along the Canadian Abyssal Plain. (As we shall see, this feature arises from an overly strong topographically steered current produced by the model.) Despite these artifacts, however, the mean ice concentration appears to be faithfully reproduced.

Figure 19 shows the year-by-year variations in ice concentration for September. [The month of March (not shown) is relatively less interesting; both models and observations find nearly complete coverage in all years, with only slight, small-scale variations between years.] As in the case of the time-mean patterns of ice concentration, the model hindcast does a respectable job in recovering the major year-to-year differences. Perhaps the most interesting of these differences is the systematic occurrence of reduced ice concentration beginning in the late 1980's. Despite some return of the ice in 1994 (in both model and the observations) surrounding Wrangel Island, the entire period from 1989 through 1996 shows lower ice concentration in the Western Arctic then in the time-average (*i.e.*,lower ice concentration for the last half of our record than for the first half).

We noted above that 1995 corresponded to a particularly warm sea surface temperature (Fig. 13). Although less apparent in the observed ice concentration for 1995, the model shows a dramatic melt-back in 1995, presumably as a consequence of the atypically warm surface forcing. The model recovers in part by 1996, but is still too ice-free in comparison with the observations. The systematic changes that are apparently occurring in the Arctic, though reproduced in the coupled model, appear to be accentuated somewhat in this simulation.

5.3 Ice thickness

Given the accompanying evidence from observations of a systematic thinning of the Arctic ice cover over the past three decades, it is not surprizing that our 15-year retrospective simulation also shows progressive loss of ice thickness with time (Fig. 20, 21). The simulated ice thickness fields for March and September both show such a trend. In March, for example, typical values of ice thickness in the early 1980's for the central Arctic tend to be about 3–4 meters, with values up to six or more meters along the Canadian/Greenland margin in some years. These modeled values of thickness are typical of those reported prior to the mid-1980's (*e.g.*, Hibler [28]). By the early 1990's, however, these values have fallen in the model hindcast to 1–2 meters and 3-4 meters, respectively. This loss of ice thickness is consistent with, though perhaps somewhat faster than, reported observations (*e.g.*, Rothrock *et al.* [45]). Similar losses are seen in September.

5.4 Ice motion

Two estimates of ice motion for the 15 Septembers encompassed in our hindcast – one from observations of buoy motion (Rigor *et al.* [44]), and that reproduced by the coupled model – are shown in Fig. 22. Note that a different color bar has been used for each; the range of speeds covered by the observed ice motion is one-half that of the range of speeds for the modeled ice motion. This mode of presentation was chosen to make both sets of vectors equally visible, since the optimally interpolated fields of observed ice (buoy) motion tend to be smaller than those modeled by about a factor of two. This is in part a reflection of the smoothing of the observed motion fields as a consequence of the optimal interpolation process, which tends to weaken any strong local flows.

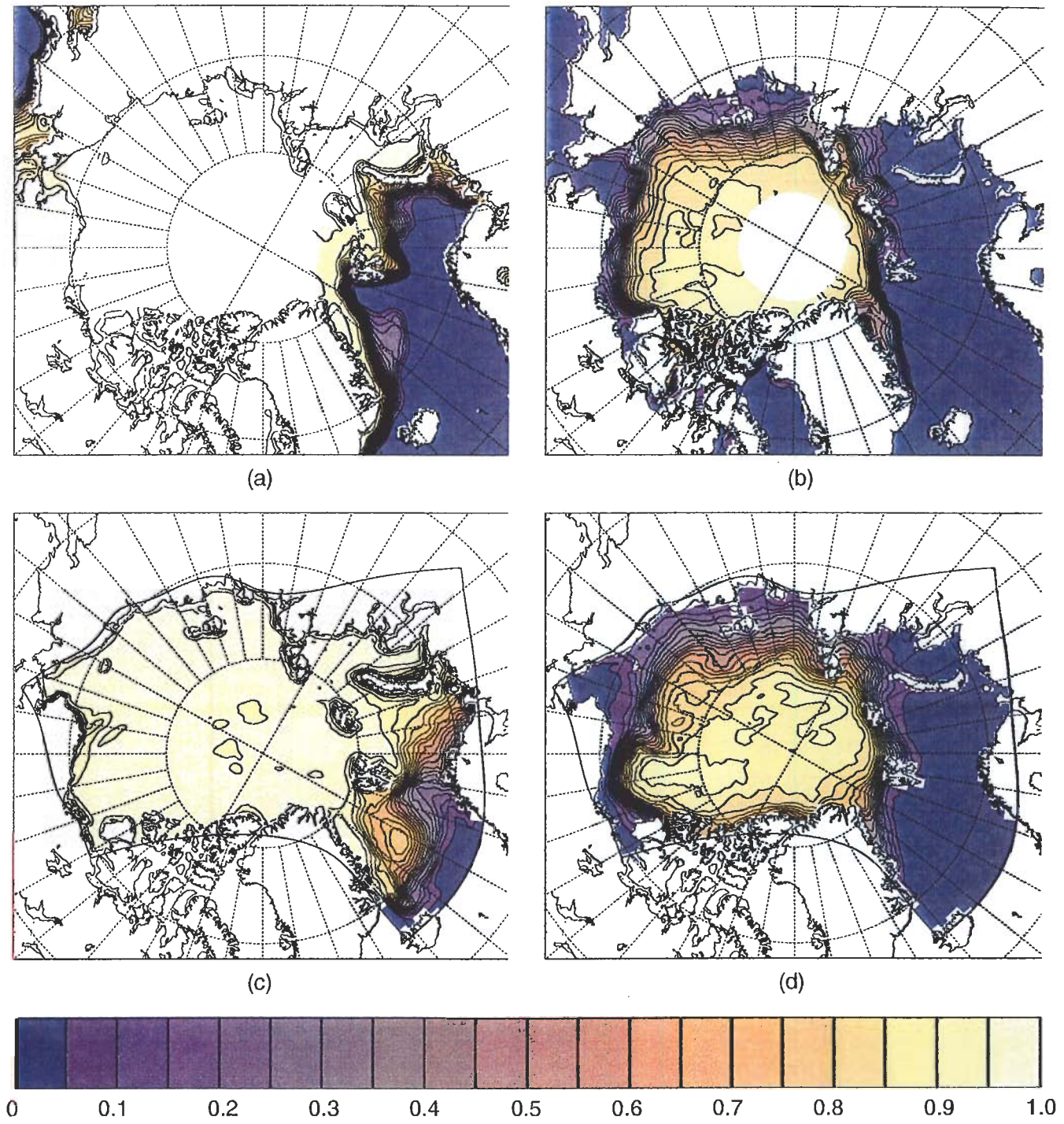

Figure 17: Time-mean (1982-1996) ice concentration in the Arctic: (a) March (observed), (b) September (observed), (c) March (model), (d) September (model).

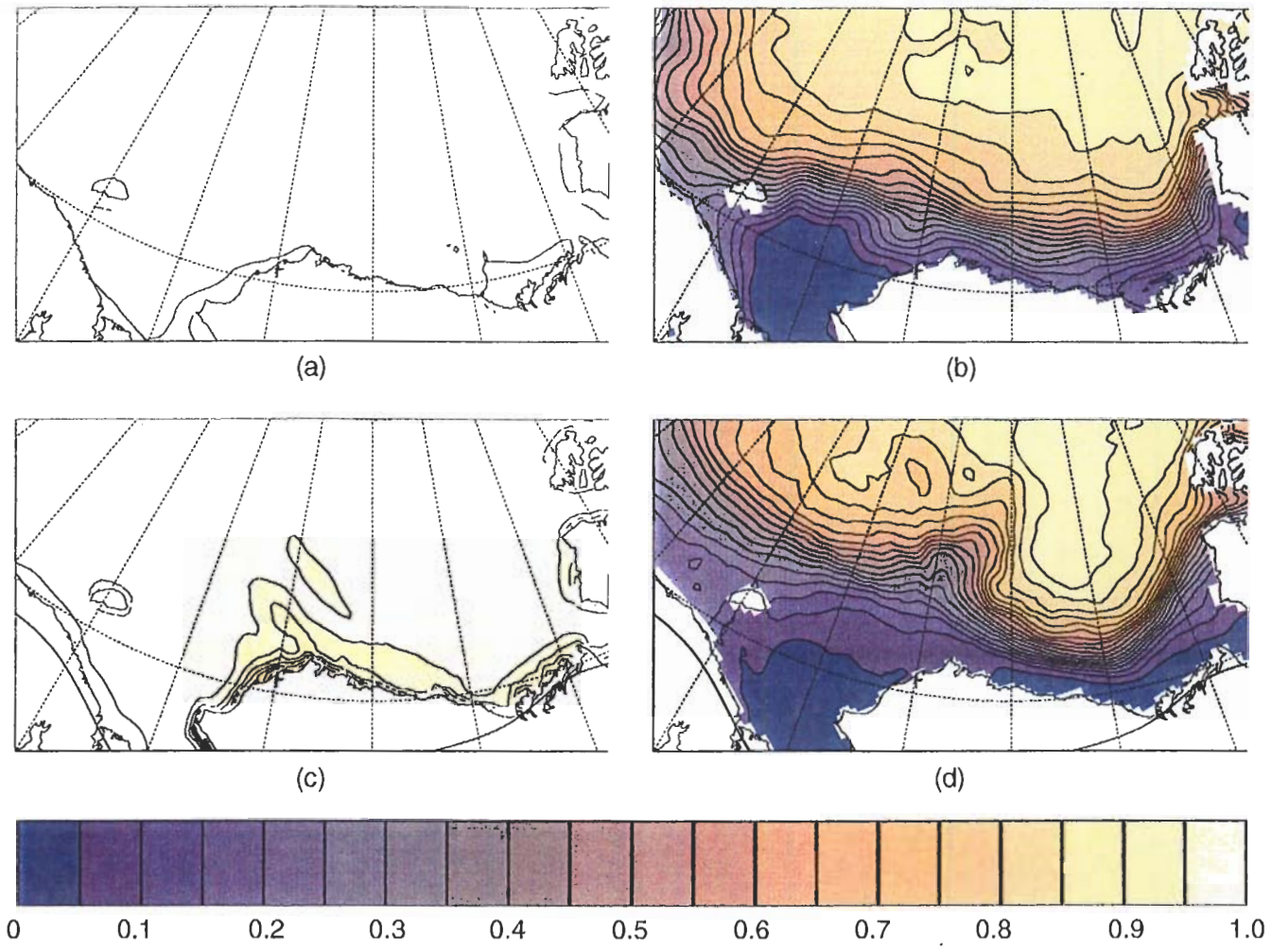

Figure 18: Time-mean (1982-1996) ice concentration in the Western Arctic: (a) March (observed), (b) September (observed), (c) March (model), (d) September (model).

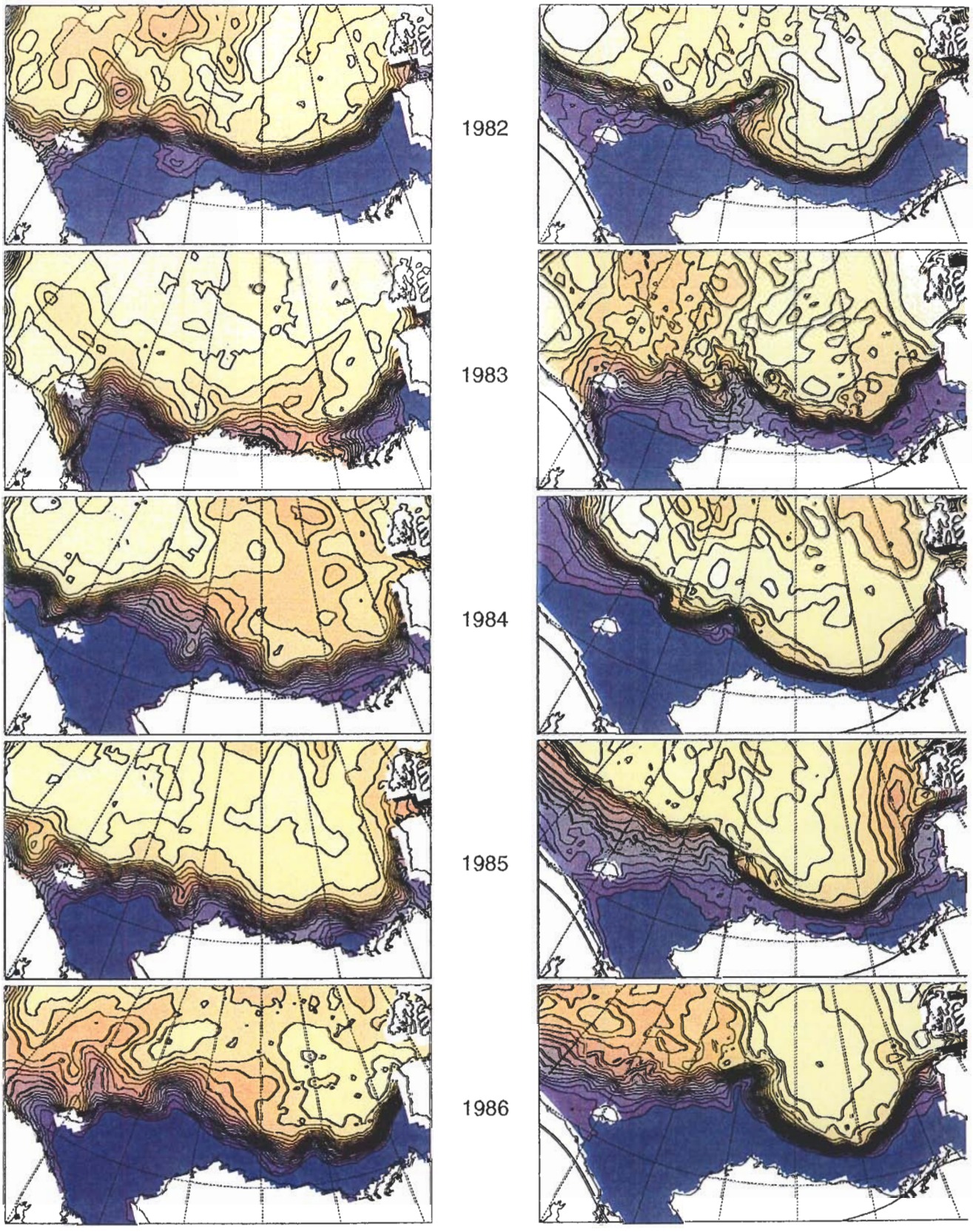

Figure 19: Ice concentration in the western Arctic Ocean for September: (left) observed, (right) model hindcast. The color contours are those used in Fig. 18.

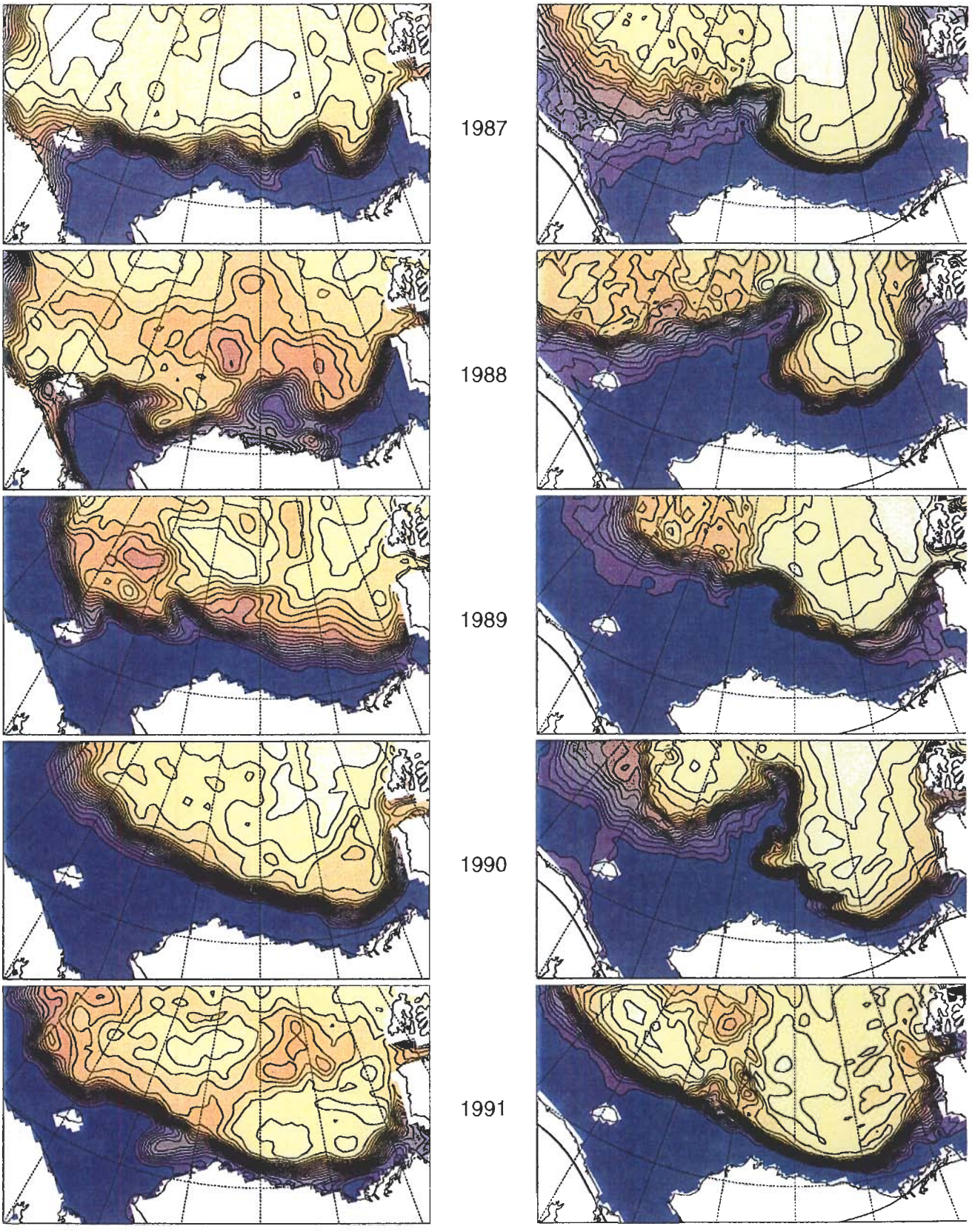

Figure 19 continued.

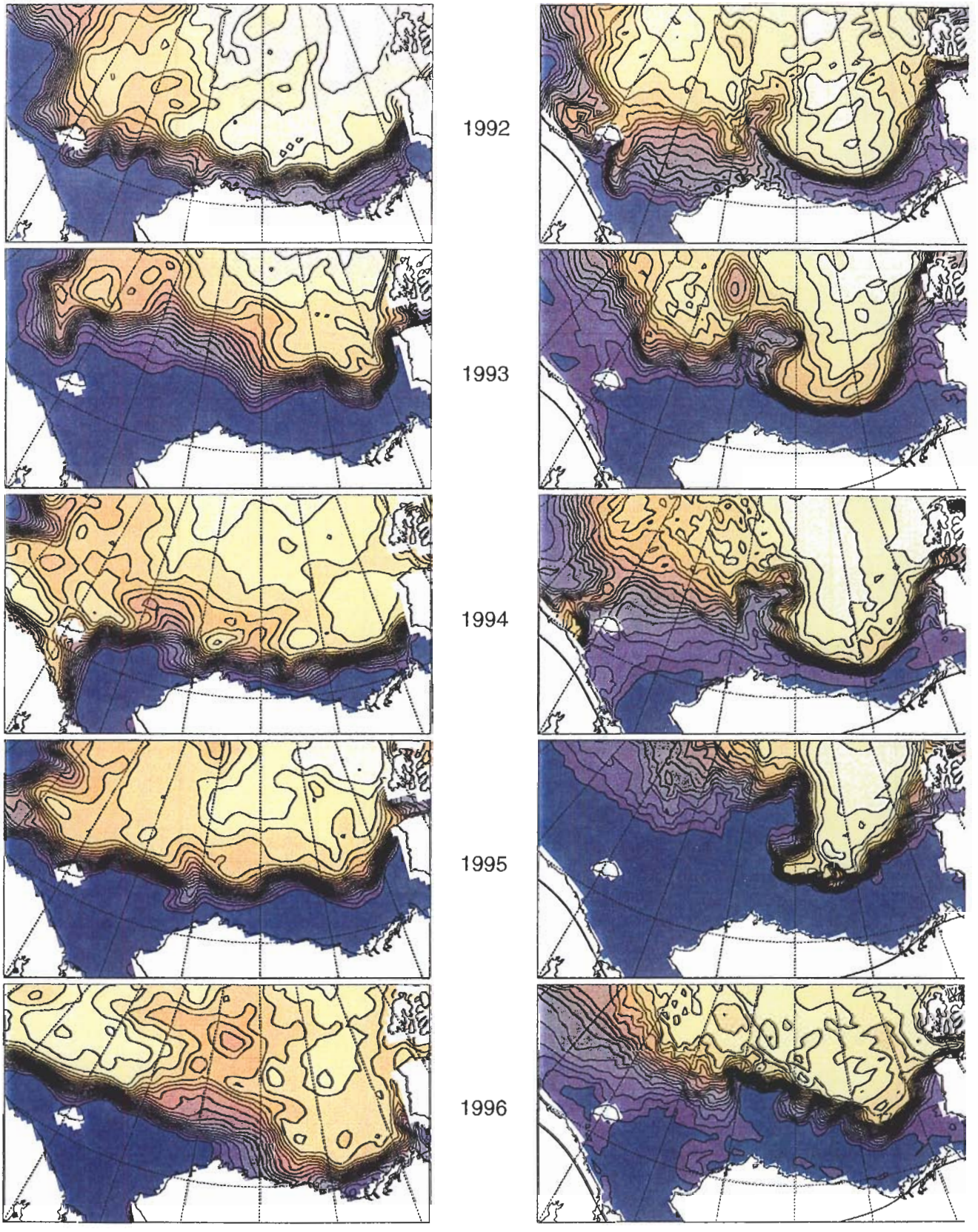

Figure 19 continued.

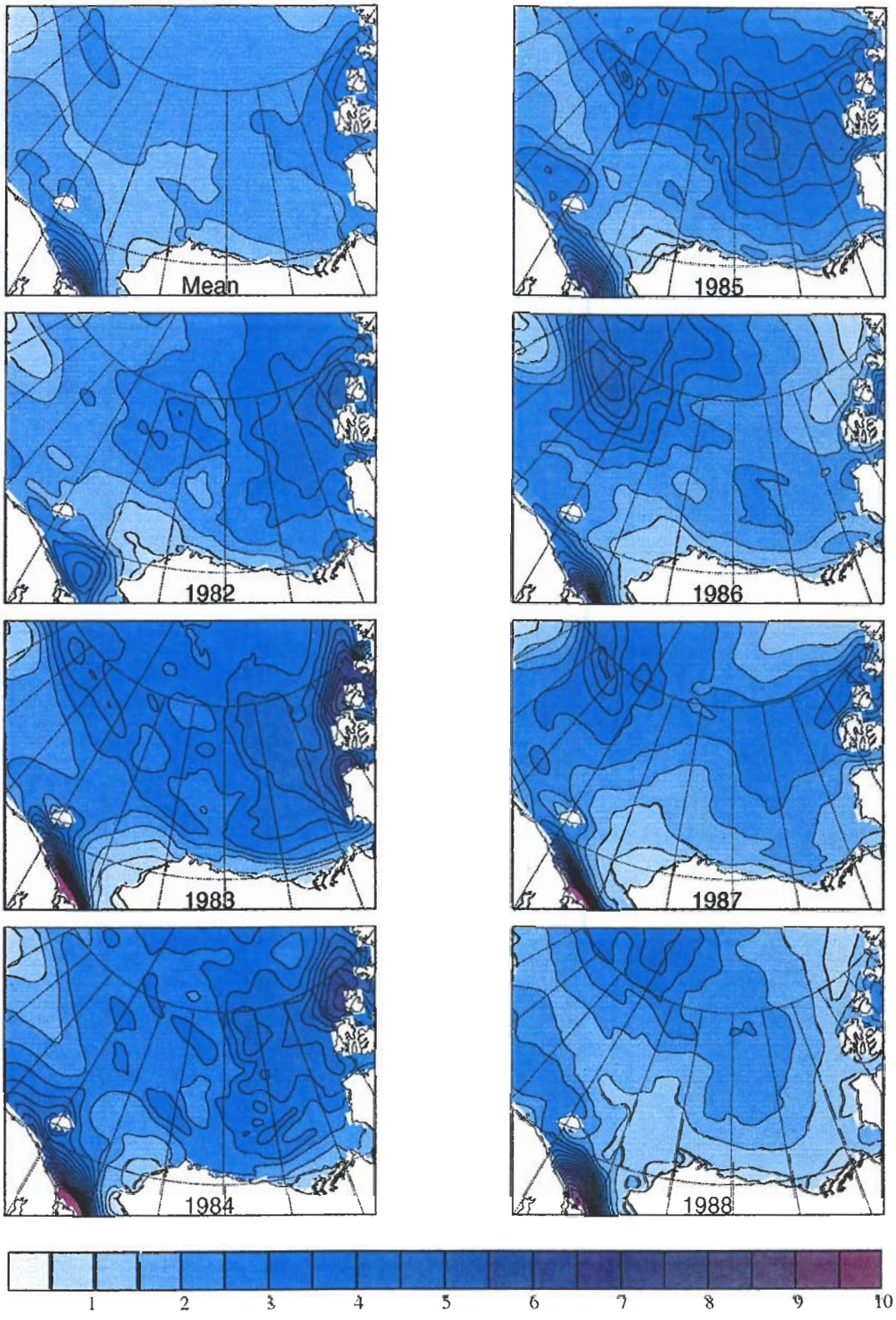

Figure 20: Model ice thickness in the western Arctic Ocean for March.

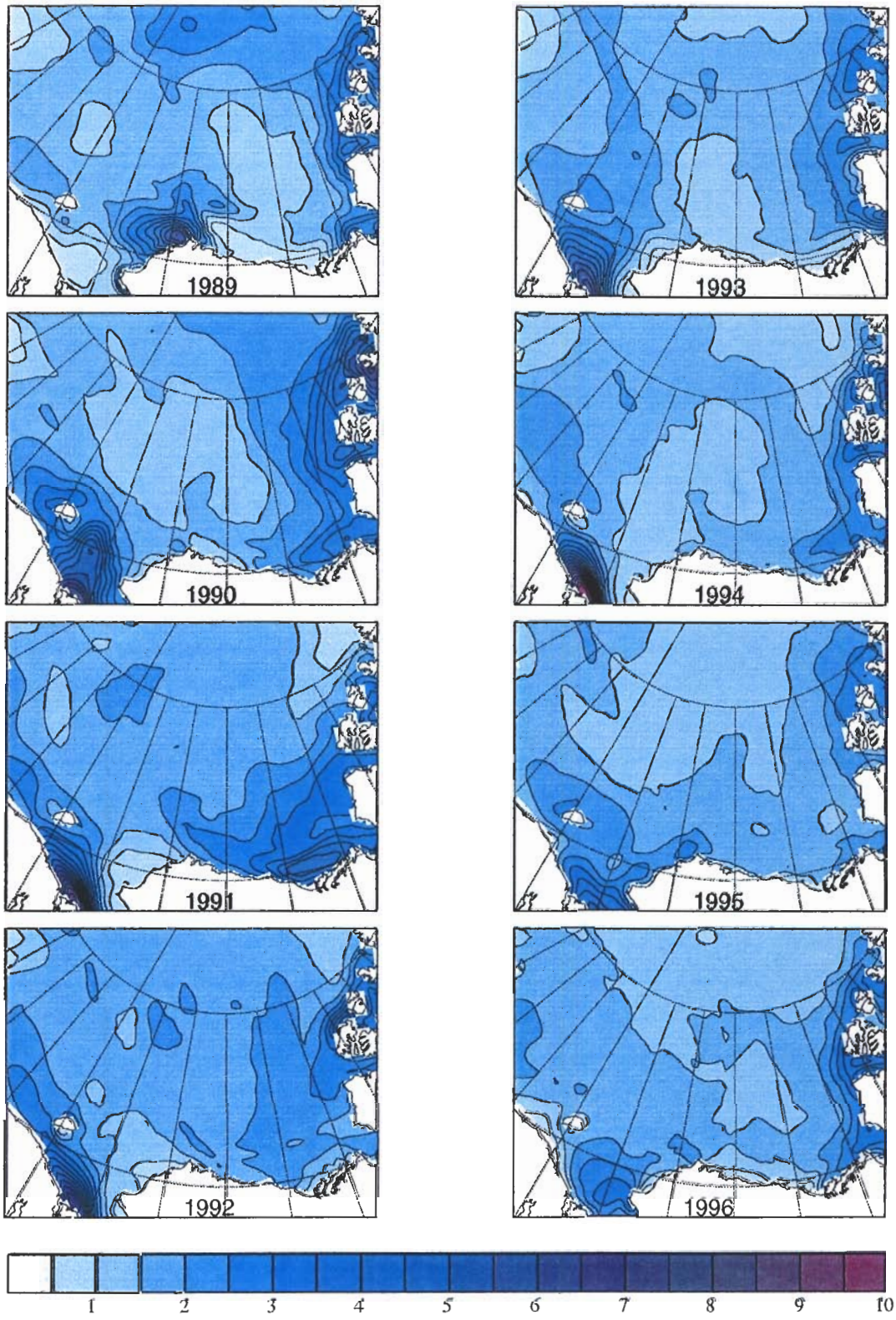

Figure 20 continued.

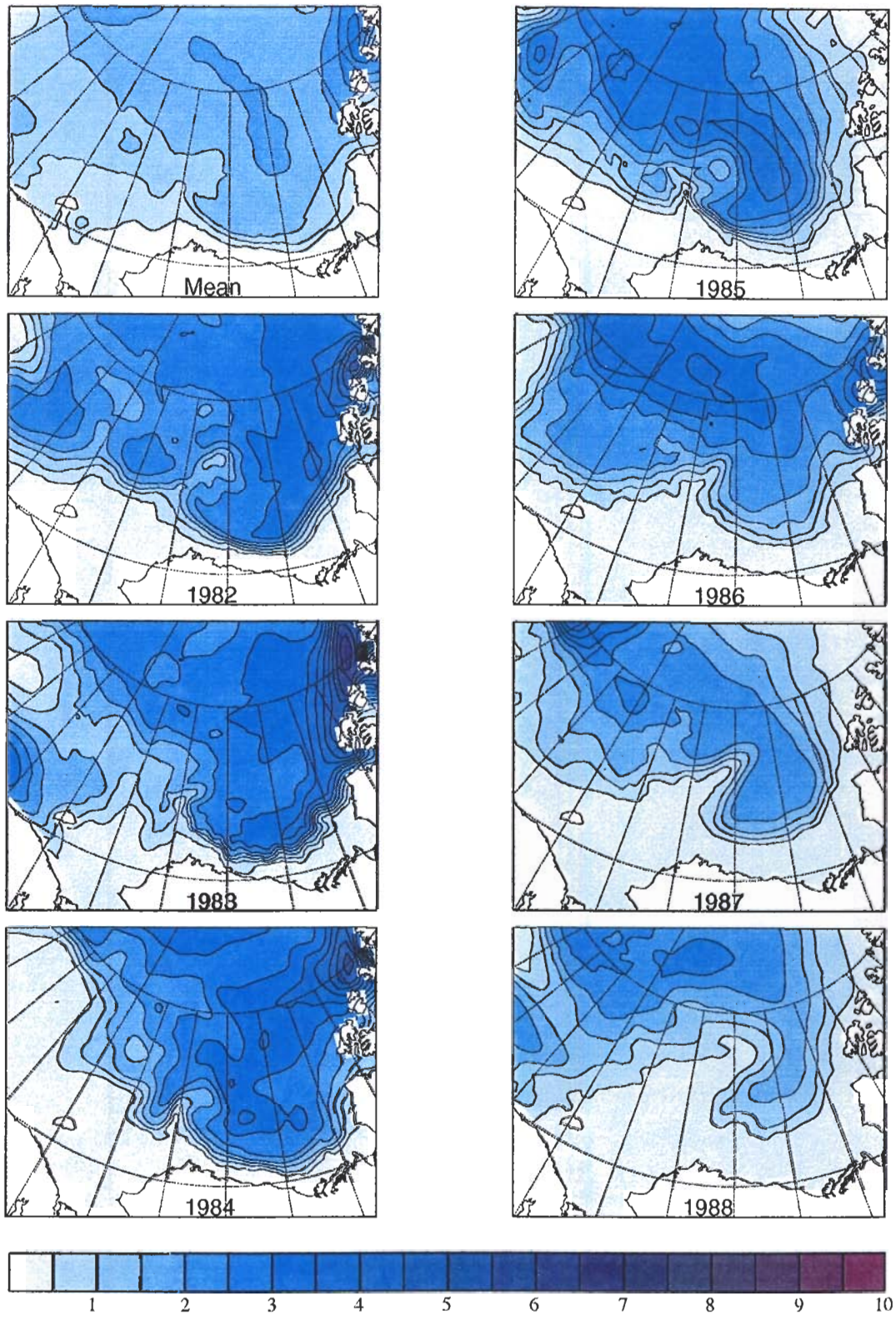

Figure 21: Model ice thickness in the western Arctic Ocean for September.

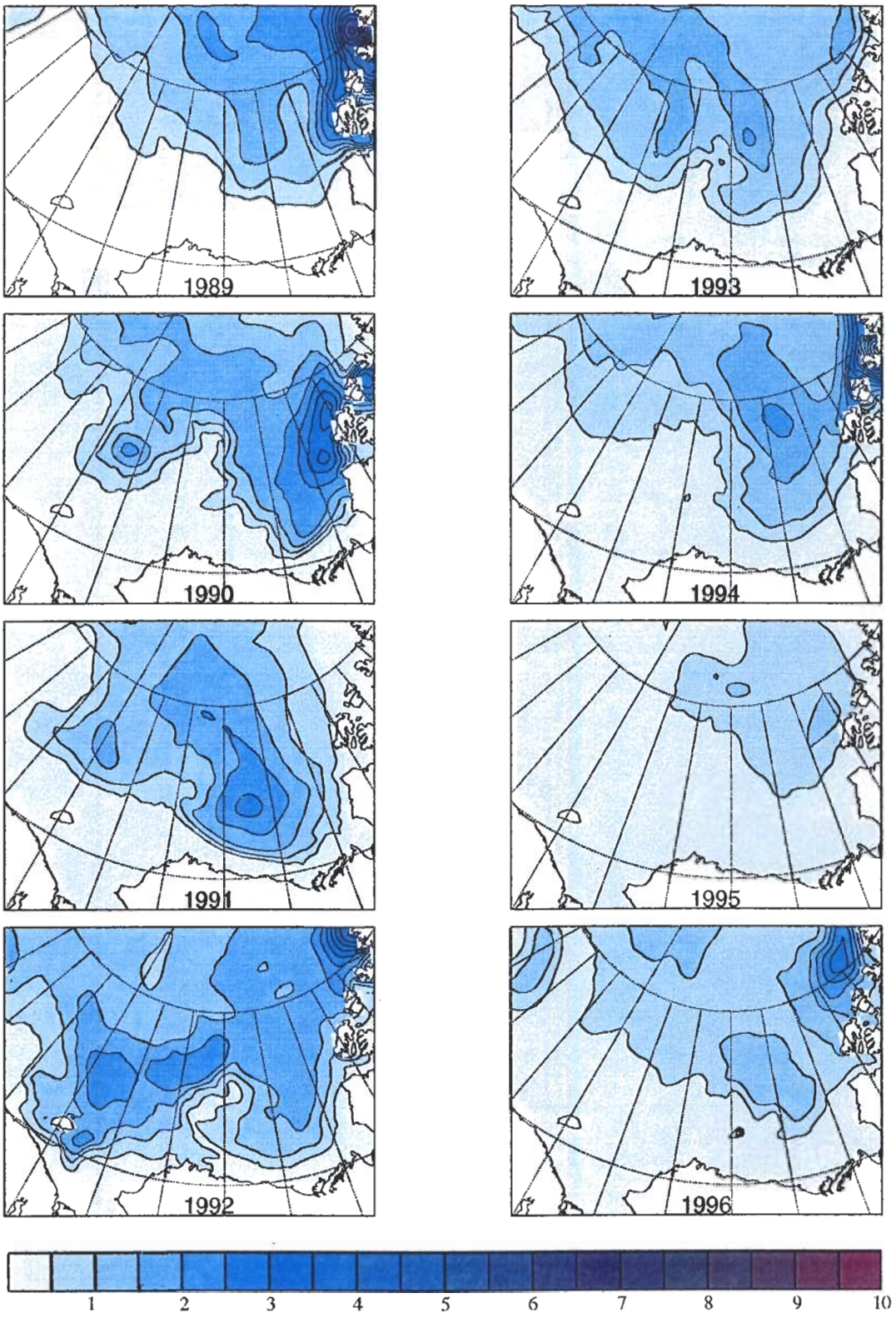

Figure 21 continued.

Nonetheless, it is also possible that the hindcast is overestimating ice motion speeds. Both sources of error are no doubt present, though it is difficult to say which is the dominant error mechanism.

With this said, it is appropriate to examine overall patterns of ice motion, which ought to be comparable despite the smoothing of the observed ice motion vectors. First looking at the large-scale patterns of ice motion, we find considerable agreement between model and observations, especially in years for which the observed buoy motions indicate either well-organized cyclonic or anti-cyclonic flow. The former occur in September of 1983, 1988 and 1994; the latter appear in 1982, 1991 and 1995. Although the flows are less well organized in many of the remaining years, there is nonetheless a high degree of similarity in the observed and modeled patterns of flow (*e.g.*, in 1984, 1987, 1989). It is fair to note also a few years in which the agreement is less good. Of these, September of 1992 and 1995 appear to show the poorest reproduction of ice motion. As you will recall, 1995 was also an anomalous year for sea surface temperature, and for ice extent in the resulting hindcast.

Given this general agreement, and allowing for some degree of spatial intensification in the hindcast flows, there nonetheless does appear to be a systematic small-scale feature in the model that has no apparent counterpart in the observations. This is a strong tendency for offshore-directed flow at Point Barrow, following the Northwind Escarpment. This tendency of the modeled circulation to follow the regional topography is not dynamically inappropriate; however, the available observations certainly suggest that the model is too tightly coupled to the bathymetry in this particular case. This tight coupling to underlying bathymetry has been noted previously in this class of terrain-following models, and may be accentuated here by the omission of sidewall buoyancy forcing (river runoff).

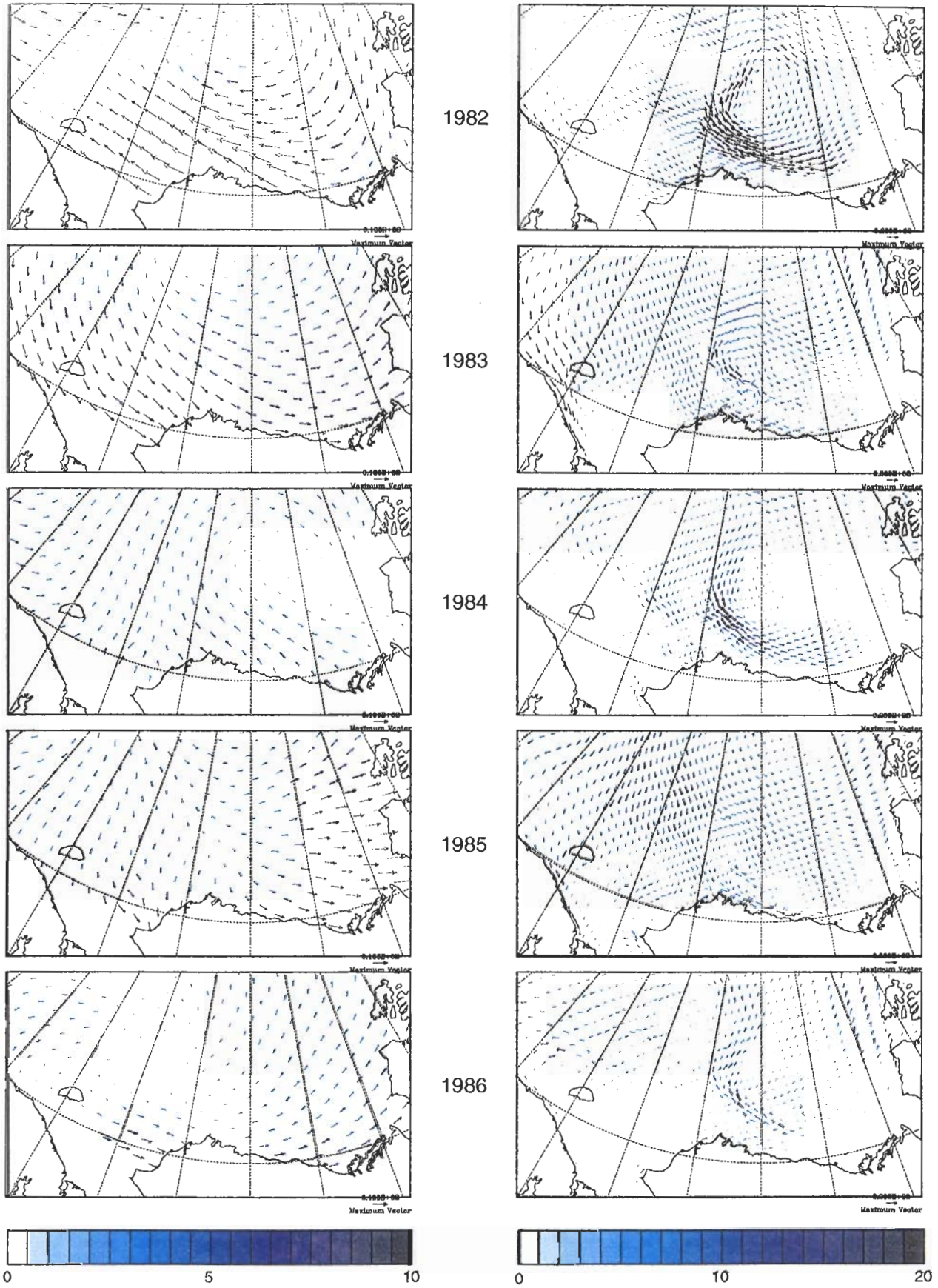

Figure 22: Ice motion (cm/s) for the month of September (1982-1996): (left) buoy-derived fields, (right) model hindcast.

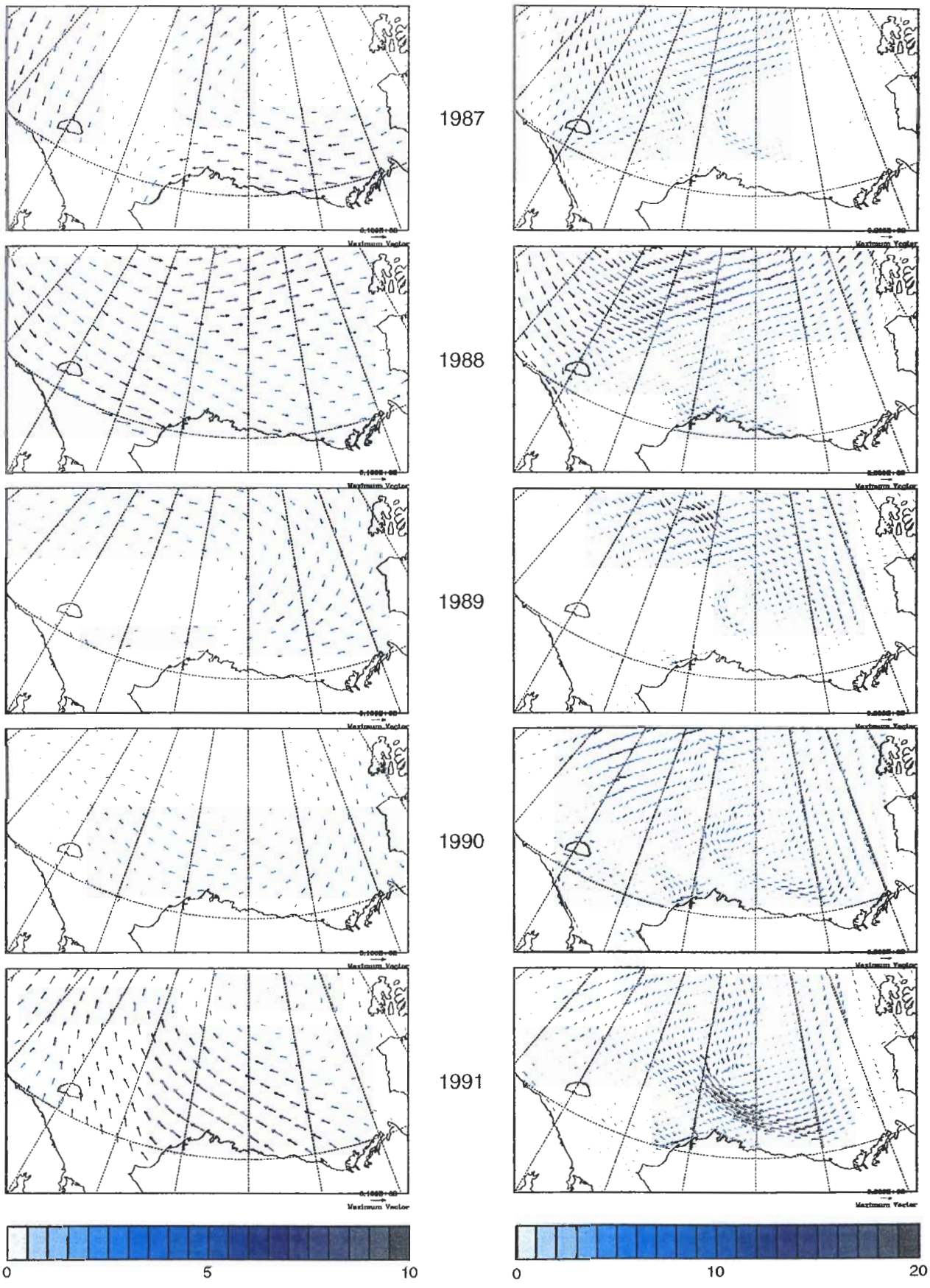

Figure 22 continued.

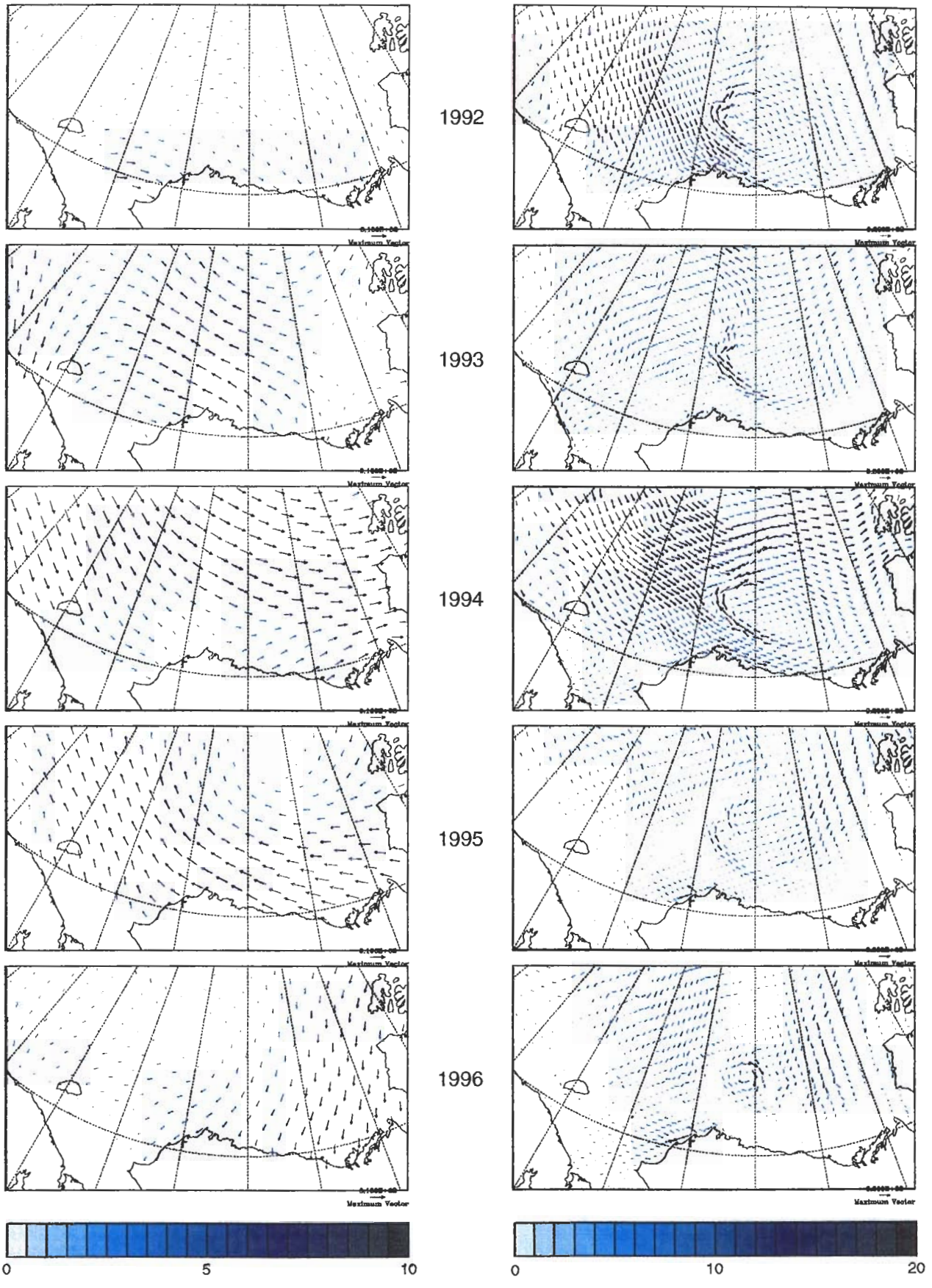

Figure 22 continued.

6 Assessment and discussion

A multi-year hindcast of coupled circulation/sea ice evolution in the Arctic Ocean has been performed using version 2 of our coupled model (Hedström [25]). Improvements from our past efforts (Hedström *et al.* [26]) include: the addition to the circulation model of an active sea surface and a state-of-the-art surface mixing parameterization (Large *et al.* [33]), the incorporation within the sea ice model of improved thermodynamics and a more robust elliptic solver for the ice mechanics, a model geometry that incorporates the entire Arctic Ocean and its full water column depth, utilization of the improved atmospheric forcing datasets described in §3, and finally the extension of the model hindcast to encompass the entire 15-year period from 1982 through 1996.

The results of 15-year coupled model hindcast are consistent with the large-scale circulation features and sea ice distributions within the Arctic Ocean, to the extent that quantitative datasets exist for validation. Importantly, the bulk properties of the sea ice distribution observed during 1982-1996 – including ice concentration, thickness and motion, and their interannual variations – are reproduced well by the coupled model. Several smaller-scale disagreements with the observations occur primarily in two regions: directly adjacent to the coastal boundary (*e.g.*) in the Western Arctic, and near the open boundary with the Atlantic Ocean. The former defect is likely caused, in part, by omission of "fast ice" in the formulation of the sea ice model. The latter is due to incomplete exchange of properties with the Atlantic Ocean due to insufficiently "open" open boundaries.

The new Path-P datasets and the resulting coupled model hindcast clearly show considerable interannual variability in atmospheric, oceanic and cryospheric variables. In addition to prominent year-to-year variations in (*e.g.*) the strength of the Beaufort Gyre and the associated sea ice motion, there are also strong progressive changes. In particular, the coupled model reproduces the systematic variations in sea ice properties – including ice concentration and thickness – noted in several recent studies (Rothrock *et al.* [45], Cavalieri *et al.* [11], Kwok [31], Smith ([49]).

Despite the overall positive appraisal we give to the coupled model and its hindcast ability, improvements in several areas are desirable, as follows:

- Improved model physics: Successive versions of our terrain-following model have been perfected since version 2 of our coupled model was implemented. These newer versions have more efficient time-stepping, better quasi-montone advection schemes, more accurate pressure gradients with associated improvements in treatment of topography, and additional capabilities for inclusion of (*e.g.*) riverine sources and tides.

- Highly parallel physics: The latest circulation models are highly parallel, allowing efficient computation of large problems.

- Enhanced resolution [O(5 *km*)] and steeper, less smoothed bathymetry: Both of these features are now possible, given the preceding improvements in model software and continuing enhancements in available computational resources.

- Ice thermodynamics with more ice categories and more vertical levels of ice temperature.

- Improved open boundary conditions: Although still a matter more of art than science, there now exist better inflow/outflow treatments that should improve exchanges with (*e.g.*) the Atlantic Ocean and Bering Sea.

- Better ridging function that is consistent with the ice rheology.

As we note, progress on models and methods that has occurred in the past few years now make many of these improvements possible. A newest coupled circulation/sea ice model incorporating all of these items has in fact been recently implemented, with a first application to the Southern Ocean.

References

[1] Jr. A. J. Semtner. A model for the thermodynamic growth of sea ice in numerical investigations of climate. *J. Phys. Oceanogr.*, 6:379–389, 1976.

[2] Jr. A. J. Semtner. Numerical simulation of the arctic ocean circulation. *J. Phys. Oceanogr.*, 6:409–425, 1976.

[3] Jr. A. J. Semtner. A numerical study of sea ice and ocean circulation in the arctic. *J. Phys. Oceanogr.*, 17:1077–1099, 1987.

[4] K. Aagaard. A synthesis of arctic ocean circulation. *Rapp. P.-V. Reun. Cons. Int. Explor. Mer*, 188:11–22, 1989.

[5] K. Aagaard and E. C. Carmack. The role of sea ice and other freshwater in the arctic circulation. *J. Geophys. Res.*, 94:14,485–14,498, 1989.

[6] AMAP. Amap assessment report: Arctic pollution issues. Technical report, Arctic Monitoring and Assessment Programme, Oslo, Norway, 1998.

[7] G. Bjork. On the response of the equilibrium thickness distribution of sea ice to ice export, mechanical deformation, and thermal forcing with application to the arctic ocean. *J. Geophys. Res.*, 97:11,287–11,298, 1992.

[8] A. F. Blumberg and G. L. Mellor. A description of a three-dimensional coastal ocean circulation model. In N. Heaps, editor, *Three-Dimensional Coastal Ocean Models.* American Geophysical Union, Washington, D.C., 1987.

[9] R. H. Bourke and R. P. Garrett. Sea ice thickness distribution in the arctic ocean. *Cold Reg. Sci. Tech.*, 13:259–280, 1987.

[10] W. J. Campbell, J. P. Gloersen, E. G. Josberger, O. M. Johannessen, P. S. Guest, N. M. Mognard, R. Shuchman, B. A. Burns, N. Lannelongue, and K. L. Davidson. Variations of mesoscale and large-scale sea ice morphology in the 1984 marginal ice zone experiment as observed by microwave remote sensing. *J. Geophys. Res.*, 92:6805–6824, 1987.

[11] D. J. Cavalieri, P. Gloersen, C. L. Parkinson, J. C. Comiso, and H. J. Zwally. Observed hemispheric asymmetry in global sea ice changes. *Science*, 278:1104–1106, 1997.

[12] D. J. Cavalieri, C. L. Parkinson, P. Gloerson, and H. J. Zwally. Sea ice concentrations from nimbus-7 smmr and dmsp ssm/i passive microwave data. Digital data available from nsidc@kryos.colorado.edu . Boulder, CO, USA: NSIDC, Distributed Active Archive Center, University of Colorado at Boulder., 1999.

[13] A. Chedin, N. A. Scott, C. Wahiche, and P. Moulineir. The improved initialization inversion method: A high resolution physical method for temperature retrievals from satellites of the tiros-n series. *J. Clim. Appl. Meteorol.*, 24:128–143, 1985.

[14] R. Colony and I. Rigor. Arctic ocean buoy program data report for 1 january 1990-31 december 1990. Technical Report APL-UW TM 10-91, Appl. Phys. Lab., Univ. of Wash., Seattle, May 1991.

[15] B. Dickson. All change in the arctic. *Nature*, 397:389–391, 1999.

[16] R. R. Dickson, J. Meincke, S.-A. Malmberg, and A. J. Lee. The great "salinity anomaly" in the northern north atlantic, 1968-1982. *Prog. Oceanogr.*, 20:103–151, 1988.

[17] G. H. Fleming. Development of a large-scale coupled sea-ice model for interannual simulations of ice cover in the arctic. Technical Report NDS-68-89-009, Naval Postgraduate School, Monterey, California, 1989.

[18] G. H. Fleming and Jr. A. J. Semtner. A numerical study of interannual ocean forcing on arctic ice. *J. Geophys. Res.*, 96:4589–4603, 1991.

[19] J. A. Francis. Improvements to tovs retrievals over sea ice and applications to estimating arctic energy fluxes. *J. Geophys. Res.*, 99:10,395–10,408, 1994.

[20] J. A. Francis and A. Schweiger. A new window opens on the arctic. *Trans. Amer. Geophys. Un.*, 81:77–83, 2000.

[21] J. M. N. T. Gray and P. D. Killworth. Stability of the viscous-plastic sea ice rheology. *J. Phys. Oceanogr.*, 25:971–978, 1995.

[22] J. M. N. T. Gray and P. D. Killworth. Sea ice ridging schemes. *J. Phys. Oceanogr.*, 26:2420–2428, 1996.

[23] D. Haidvogel, J. Wilkin, and R. Young. A semi-spectral primitive equation ocean circulation model using vertical sigma and orthogonal curvilinear horizontal coordinates. *J. Comp. Phys.*, 94:151–184, 1991.

[24] S. Hakkinen. An arctic source for the great salinity anomaly: a simulation of the arctic ice-ocean system for 1955-1975. *J. Geophys. Res.*, 98:16,397–16,410, 1993.

[25] K. S. Hedstrom. Technical manual for a coupled sea-ice/ocean circulation model (version 2). Technical report, Institute of Marine and Coastal Sciences, Rutgers University, New Brunswick, NJ, April 2000. OCS Study MMS 2000-047.

[26] K. S. Hedstrom, D. B. Haidvogel, and S. Signorini. Model simulations of ocean/sea-ice interaction in the western arctic in 1983. Technical report, Institute of Marine and Coastal Sciences, Rutgers University, New Brunswick, NJ, March 1995. OCS Study MMS 95-0001.

[27] W. D. Hibler, III. A dynamic thermodynamic sea ice model. *J. Phys. Oceanogr.*, 9:815–846, 1979.

[28] W. D. Hibler, III. Documentation for a two-level dynamic thermodynamic sea ice model. Technical report, USACRREL, Hanover, NH, 1980. Special Report 80-8.

[29] W. D. Hibler, III and K. Bryan. A diagnostic ice-ocean model. *J. Phys. Oceanogr.*, 17:987–1015, 1987.

[30] L. Kantha and G. L. Mellor. A two-dimensional coupled ice-ocean model of the bering sea marginal ice zone. *J. Geophys. Res.*, 94:10921–10935, 1989.

[31] R. Kwok. Recent changes in arctic ocean sea ice motion associated with the north atlantic oscillation. *Geophys. Res. Lett.*, 27:775–778, 1999.

[32] R. Kwok and D. A. Rothrock. Variability of fram strait ice flux and north atlantic oscillation. *J. Geophys. Res.*, 104:5177, 1999.

[33] W. G. Large, J. C. McWilliams, and S. C. Doney. Oceanic vertical mixing: a review and a model with a nonlocal boundary layer parameterization. *Rev. Geophys.*, 32:363–403, 1994.

[34] J. A. Maslanik, M. C. Serreze, and T. Agnew. On the record reduction in 1998 western arctic sea-ice cover. *Geophys. Res. Lett.*, 26:1905–1908, 1999.

[35] J. A. Maslanik, M. C. Serreze, and R. G. Barry. Recent decreases in arctic summer ice cover and linkages to atmospheric circulation anomalies. *Geophys. Res. Lett.*, 23:1677–1680, 1996.

[36] G. L. Mellor and L. Kantha. An ice-ocean coupled model. *J. Geophys. Res.*, 94:10,937–10,954, 1989.

[37] G. L. Mellor and T. Yamada. A hierarchy of turbulence closure models for planetary boundary layers. *J. Atmos. Sci.*, 31:1791–1806, 1974.

[38] N. Nakamura and A. H. Oort. Atmospheric heat budgets of the polar regions. *J. Geophys. Res.*, 93:9510–9524, 1988.

[39] J. E. Overland, J. M. Adams, and N. A. Bond. Decadal variability of the aleutian low and its relation to high-latitude circulation. *J. Climate*, 12:1542–1548, 1999.

[40] C. L. Parkinson. Interannual variability of the spatial distribution of sea ice in the north polar region. *J. Geophys. Res.*, 96:4791–4801, 1991.

[41] C. L. Parkinson and W. M. Washington. A large-scale numerical model of sea ice. *J. Geophys. Res.*, 84:6565–6575, 1979.

[42] S. Piacsek, R. Allard, and A. Warn-Varnas. Studies of the arctic ice cover and upper ocean with a coupled ice-ocean model. *J. Geophys. Res.*, 96:4631–4650, 1991.

[43] I. G. Rigor, R. L. Colony, and S. Martin. Variations in surface air temperature observations in the arctic, 1979-1997. *J. Climate*, 13:896–914, 2000.

[44] I. G. Rigor, J. M. Wallace, and R. L. Colony. On the response of sea ice to the arctic oscillation. *J. Climate (to appear)*, 2001.

[45] D. A. Rothrock, Y. Yu, and G. A. Maykut. Thinning of the arctic sea-ice cover. *Geophys. Res. Lett.*, 26:3469–3472, 1999.

[46] A. J. Schweiger, R. W. Lindsay, J. R. Key, and J. A. Francis. Arctic clouds in multiyear satellite data sets. *Geophys. Res. Lett.*, 26:1845–1848, 1999.

[47] N. A. Scott, A. Chedin, R. Armante, J. Francis, C. Stubenrauch, J.-P. Chaboureau, F. Chevallier, C. Claud, and F. Cheruy. Characteristics of the tovs pathfinder path-b dataset. *Bulletin of the Am. Meteor. Soc.*, 80:2679–2701, 1999.

[48] M. C. Serreze, F. Carsey, R. G. Barry, and J. C. Rogers. Icelandic low cyclone activity: climatological features, linkages with the nao, and relationships with recent changes in the northern hemisphere circulation. *J. Climate*, 10:453–464, 2000.

[49] D. M. Smith. Recent increase in the length of the melt season of perennial arctic sea ice. *Geophys. Res. Lett.*, 25:655–658, 1998.

[50] M. Steele, G. L. Mellor, and M. G. McPhee. Role of the molecular sublayer in the melting or freezing of sea ice. *J. Phys. Oceanogr.*, 19:139–147, 1989.

[51] D. W. J. Thompson and J. M. Wallace. The arctic oscillation signature in the wintertime geopotential height and temperature fields. *Geophys. Res. Lett.*, 25:1297–1300, 1998.

[52] A. S. Thorndike. A toy model linking atmospheric thermal radiation and sea ice growth. *J. Geophys. Res.*, 97:9401–9410, 1992.

[53] A. S. Threshnikov and G. I. Baranov. Water circulation in the arctic basin. Technical report, Israel Program for Scientific Translations Ltd., 1973.

[54] L. Timokhov and F. Tannis. Environmental working group joint u.s.-russian atlas of the arctic ocean - winter period. Technical report, Environmental Research Institute of Michigan and NSIDC, 1997.

[55] J. E. Walsh, W. L. Chapman, and T. L. Shy. Recent decrease of sea level pressure in the central arctic. *J. Climate*, 9:480–486, 1996.

[56] J. E. Walsh, W. D. Hibler, III, and B. Ross. Numerical simulation of northern hemisphere sea ice variability, 1951-1980. *J. Geophys. Res.*, 90:4847–4865, 1985.

[57] J. E. Walsh and C. M. Johnson. An analysis of arctic sea ice fluctuations. *J. Phys. Oceanogr.*, 9:580–591, 1979.

[58] J. Wang and M. Ikeda. Arctic oscillation and arctic sea-ice oscillation. *Geophys. Res. Lett.*, in press, 2000.